

A Hubble Space Telescope Optical and Ground-Based Near-Infrared
Study of the Giant Nuclear Ring in ESO 565-11

Ronald J. Buta – University of Alabama

D. A. Crocker – University of Alabama

G. G. Byrd – University of Alabama

Deposited 06/21/2019

Citation of published version:

Buta, R., Crocker, D., Byrd, G. (1999): A Hubble Space Telescope Optical and Ground-Based Near-Infrared Study of the Giant Nuclear Ring in ESO 565-11. *The Astronomical Journal*, 118(3). DOI: [10.1086/301085](https://doi.org/10.1086/301085)

A HUBBLE SPACE TELESCOPE OPTICAL AND GROUND-BASED NEAR-INFRARED STUDY OF THE GIANT NUCLEAR RING IN ESO 565-11¹

R. BUTA,^{2,3} D. A. CROCKER,² AND G. G. BYRD²

Received 1999 May 17; accepted 1999 August 9

ABSTRACT

We present multiband Wide Field Planetary Camera 2 images of the central regions of ESO 565-11, a peculiar southern barred galaxy recently shown to have the largest known example of a circumnuclear starburst ring. We also present ground-based near-infrared *H*-band imaging and photometry of the galaxy. The results provide an interesting picture of the star-forming ring and its environment. Dust connected with the nuclear ring lies mainly in a symmetric two-armed spiral pattern. More than 700 point sources, mostly unresolved clusters, lie on a highly elliptical ring whose major axis is rotated by more than 20° from that of the isophotes of the background starlight. The luminosity function of these clusters follows a power law with slope $a = -2.18 \pm 0.06$, typical of young cluster systems. Most of the clusters lie in the age range 4–6 Myr, and most may be metal-rich compared with the Sun. The nuclear ring is still clearly seen in the *H* band, revealing a knotty appearance indicating that young stars continue to have a significant impact on its brightness in this passband. Numerical simulations are used to show that the nuclear ring of ESO 565-11 has likely formed between two allowed inner Lindblad resonances with the relatively weak primary bar. The results indicate that the excessive size of the ring may be due to an extended hump in the variation of the parameter $\Omega - \kappa/2$ with radius. The extreme elongation of the ring and its misalignment with the bar may indicate that it is in an early phase of development. At later times, the simulations suggest that the ring could evolve to a rounder shape. The models do not account for star formation or gas recycling.

Key words: galaxies: individual (ESO 565-11) — galaxies: kinematics and dynamics — galaxies: photometry — galaxies: structure

1. INTRODUCTION

Nuclear rings of intense star formation are well-known features of early to intermediate Hubble type barred spiral galaxies (Morgan 1958; Burbidge & Burbidge 1960; Sérsic & Pastoriza 1965, 1967; Sandage 1961; Rubin, Ford, & Peterson 1975; Buta & Crocker 1993; Sellwood & Wilkinson 1993; plus many other references listed by Buta & Combes 1996). These small rings, typically less than 10" in angular radius, are sometimes the only place where significant levels of star formation are taking place in a galaxy (e.g., NGC 4314; see Benedict, Smith, & Kenney 1996). The high star formation rates and dust found in and around some nuclear rings makes them unusually prominent at radio continuum and infrared wavelengths (see, e.g., Hawarden et al. 1986; García-Barreto et al. 1991; Wilson et al. 1991; Combes et al. 1992; Forbes et al. 1994). Fewer than 100 examples are currently known (see Buta & Crocker 1993; Buta & Combes 1996), and it is clear from the examples studied in detail so far that the rings have a wide range of intrinsic properties.

Nuclear rings get their name from their close proximity to the nucleus of a barred galaxy, where in early photographic images they were typically overexposed. The rings are

usually distinct from larger features known as inner rings—which envelop the bar of a barred spiral—and outer rings—which are about twice the diameter of the bar. The average diameter of nuclear rings in barred spirals, deduced from a sample of 20 objects, is 1.5 kpc on a distance scale where $H_0 = 75 \text{ km s}^{-1} \text{ Mpc}^{-1}$ (Buta & Crocker 1993). The true frequency of the features is unknown, but new examples are turning up regularly (e.g., Arnaboldi et al. 1995; Contini, Davoust, & Considère 1995; Smith et al. 1995; Contini et al. 1997; Vega Beltrán et al. 1998; Díaz et al. 1999), and it is likely that they are common features of normal barred galaxies.

What makes these rings of great interest at the present time is that they represent areas in galaxies where very special conditions for star formation can develop (Elmegreen 1994). The special conditions can lead to the formation of extremely luminous star clusters lining the rings, which has led to the suggestion that the environment is conducive to forming new globular clusters much as in some complex interacting systems (Barth et al. 1995; Maoz, Sternberg, & Ho 1998; Whitmore & Schweizer 1995; Carlson et al. 1998; Schweizer 1999). Although the formation of clusters in an interacting system is a complex problem of merger dynamics, in barred galaxies the clusters most likely result from the normal gas inflow in a barred potential, coupled with resonant dynamics (Schwarz 1984; Combes & Gerin 1985; Combes 1993; Byrd et al. 1994; Knapen et al. 1995a, 1995b; Sakamoto et al. 1995; Knapen 1999). The rings point to the frequent existence of inner Lindblad resonances in barred galaxies (see, e.g., Telesco, Dressel, & Wolstencroft 1993; Piner, Stone, & Teuben 1995; Salo et al. 1999) and occasionally include secondary bars (Buta & Crocker 1993; Shaw et al. 1993; Wozniak et al. 1995; Friedli 1996). The occurrence of these features in

¹ Based on observations with the NASA/ESA *Hubble Space Telescope*, obtained at the Space Telescope Science Institute, which is operated by the Association of Universities for Research in Astronomy (AURA), Inc., under NASA contract NAS 5-26555.

² Department of Physics and Astronomy, University of Alabama, Box 870324, Tuscaloosa, AL 35487-0324.

³ Visiting Astronomer, Cerro Tololo Inter-American Observatory, National Optical Astronomy Observatories, operated by AURA, Inc., under cooperative agreement with the National Science Foundation.

some active galaxies has led to attempts to determine whether bar dynamics has an impact on the fueling of active galactic nuclei (e.g., Shlosman, Frank, & Begelman 1989; Axon & Robinson 1996; Colina et al. 1997). The short time-scales in the central kiloparsec of a barred galaxy, as well as the high molecular gas masses and densities achieved, also likely lead to episodic bursts of star formation rather than continuous star-forming activity (e.g., Hummel, van der Hulst, & Keel 1987; Telesco et al. 1993; Elmegreen 1994; Schinnerer et al. 1997; Smith et al. 1999; Kohno, Kawabe, & Vila-Vilaró 1999).

Other aspects of nuclear rings that make them important topics for detailed study is the way their morphology and that of their surroundings are so easily tied to barred galaxy dynamics. For example, Kenney et al. (1992) showed that the CO emission in the bar region of some nuclear-ringed galaxies has two bright peaks at the inner ends of leading bar dust lanes. The phenomenon may be connected with orbit crowding near the inner Lindblad resonance (ILR) region of the bar, where inward-flowing gas intersects the nuclear ring. Knapen et al. (1995a, 1995b) also identified structures attributable to ILR dynamics in the region of the nuclear ring/spiral of M100. Near the ends of a small nuclear bar inside the ring/spiral region, leading armlets were identified in the *K* band that can be explicitly tied to dynamics in the region of an inner inner Lindblad resonance (IILR; see Sakamoto et al. 1995 and references therein). Recent observations of the kinematics of the ionized and molecular gas in the core of M100 (Knapen et al. 2000) provide further support to the existence of a double inner Lindblad resonance around the nuclear ring/spiral structure. Finally, the generally oval shapes of nuclear rings, their typical misalignment with the primary bar, the existence of double nuclear rings, the presence of distinct spiral structure outside them, and the existence of both leading and trailing secondary bars within them all argue for a connection with the inner Lindblad resonance regions of barred spiral galaxies (Schweizer 1980; Buta & Crocker 1993; Wozniak et al. 1995; Crocker, Baugus, & Buta 1996; Kenney, Benedict, & Friedli 1998).

Studies of individual nuclear rings are essential for a better understanding of the role they play in the evolution of normal galaxies. However, the small angular sizes of most nuclear rings make them difficult to study from ground-based observations, at least at optical wavelengths. By the same token they are very amenable to study through *Hubble Space Telescope* (*HST*) Wide Field Planetary Camera 2 (WFPC2) observations. Examples imaged thus far (see Barth et al. 1995, 1996; Phillips et al. 1996; Benedict et al. 1998; Maoz et al. 1998) reveal a wealth of intricate detail in dust lanes and star-forming regions, showing, in particular, that features classified as nuclear rings from the ground are in fact tightly wrapped spirals in some cases. Few examples have been observed over a range of *HST* filters, but a comparison of structure at long and short wavelengths could shed light on the star formation processes in the rings and, in particular, on the nature of ring clusters.

A particularly interesting case of a nuclear ring was described by Buta, Purcell, & Crocker (1995, hereafter BPC), who studied the feature seen in the nearly face-on, peculiar southern barred galaxy ESO 565-11 (Buta & Crocker 1991). The nuclear ring of this galaxy is exceptional in that it is the largest known example, being 5 kpc in linear

diameter compared with an average of only 1.5 kpc ($H_0 = 75$). The ring also appears to be the site of a recent starburst and is lined by at least 10 giant H II regions or complexes. Nearly 80% of the H α emission from the galaxy comes from the ring region. BPC could not study the ring in much detail, however, because at the distance of 60 Mpc the feature is poorly resolved from the ground. Although many excellent nuclear rings are found in galaxies much closer to us, the feature seen in ESO 565-11 is a good case for a high-resolution study because the ring presents the most extreme intrinsic elongated shape of any nuclear ring. The feature is also significantly misaligned with the primary bar of the galaxy. These characteristics provide us with an opportunity to examine whether sequential star formation takes place in the ring, since the misalignment in conjunction with gravity torques could lead to secular evolution of the mass distribution of aging ring populations. *HST* was needed to distinguish this possibility by allowing us to separate the youngest population of clusters from the evolved stellar background.

We observed the galaxy with *HST* in order to map the detailed structure in and near the ring, such as dust lanes, shock fronts, and star-forming complexes, from the mid-UV to the *I* band as a way to examine the process of star formation in the resonance region and to connect the morphology to dynamics. We also imaged the galaxy in a near-infrared passband, the Johnson *H* band at 1.65 μm , from the ground to derive the gravitational potential in the disk and to determine the probable dynamical resonance associated with the nuclear ring. The data are used to determine the luminosity function of massive star clusters in the ring, the rate of massive star formation, the nature of star formation in the ring (episodic or continuous?), and other aspects of the ring's structure that can be connected to periodic orbit characteristics, pattern speed, and bar strength. The observations are described in § 2 and are connected to previous ground-based work in § 3. The analysis of the ring clusters is covered in §§ 4 and 5. Numerical simulations are described in § 6.

2. OBSERVATIONS

The *HST* observations of ESO 565-11 were secured on 1997 May 1 with WFPC2. The center of the galaxy was placed within the Planetary Camera (PC) section, and it is only this part that we focus on here. Five filters were used to observe the galaxy: F255W, F336W, F439W, F555W, and F814W. The latter four filters are intended to approximate the Johnson *U*, *B*, *V* and Cousins *I* photometric systems, respectively, while F255W is a mid-ultraviolet filter. The total exposure times were 1400 s for F255W and F336W, 2000 s for F439W, and 600 s each for F555W and F814W. The observations were made in a CR-SPLIT mode to facilitate removal of cosmic rays. After receiving the standard pipeline preprocessed images, the separate images were corrected for bad pixels and columns using STSDAS routine WFIXUP, and then the images for each filter were combined using STSDAS routine CRREJ. The latter routine was very effective in removing most of the cosmic rays; any remaining ones were removed using the IRAF⁴ routine IMEDIT. The gain used was 7 e^- ADU⁻¹ and the read noise was 5.2 e^- .

⁴ IRAF is distributed by the National Optical Astronomy Observatories.

The *H*-band observations of ESO 565-11 were obtained with the CTIO Infrared Imager (CIRIM) attached to the 1.5 m telescope on 1996 February 8. Images were obtained with the array operated at a bias of 900 mV and a gain of $9 e^- \text{ADU}^{-1}$. The total exposure time of 20 minutes was sufficient to detect the faint outer pseudoring at *H* and gave high signal-to-noise ratio in the inner ring/lens region and the bar region. Other details of the observations were the same as described by Buta & Purcell (1998) and Buta et al. (1998) and are not repeated here. Calibration of the final *H*-band image after flat-fielding and sky subtraction was established using three standard stars from Elias et al. (1982).

3. THE STRUCTURE OF ESO 565-11

3.1. Summary of Previously Published Ground-based Observations

The initial published ground-based images of ESO 565-11 were presented by Buta & Crocker (1991), who noted the unusual candlepin bar, the very faint outer pseudoring, the bright inner pseudoring and oval lens, and in particular the spectacular nuclear ring. Buta & Crocker (1993) found that the nuclear ring has the largest intrinsic linear diameter (3.5 times the average) among the more than 60 known examples of nuclear rings. BPC used both photometric and kinematic data to establish that the inclination of the galaxy is probably no more than 33° , indicating that the apparent axis ratio of 0.55 for the nuclear ring is close to the true value. This would be extreme because most nuclear rings have an intrinsic axis ratio in the range 0.7 to 1.0, with a likely average around 0.9 (Buta 1984; Buta & Crocker 1993). The low inclination also means that the apparent 60° misalignment between the bar axis and the inner ring/lens major axis is nearly intrinsic, which is unusual because statistics of apparent relative bar and inner ring position angles favor alignment as the rule (Buta 1995; see also Buta & Purcell 1998; Buta et al. 1998). Thus, not only does the nuclear ring have extreme properties, but the misalignment also sets the galaxy apart from normal resonance ring galaxies.

Buta & Crocker (1991, 1993) showed that the nuclear ring of ESO 565-11 contains at least nine blue “knots” arranged along an approximately east-west oval having a diameter of $17''$. BPC estimated the apparent magnitudes of the “knots” to be in the range $B = 18\text{--}20$ with average colors $\langle B - V \rangle = 0.05$ and $\langle V - I \rangle = 0.45$, indicating that these objects are likely to be associations of massive stars less than 10 million years old. The young ages are confirmed by BPC’s detection of 13 discrete $H\alpha$ emission sources lining the ring. These sources account for 77% of the total $H\alpha$ emission from the galaxy and on average are more luminous than the $H\text{ II}$ regions found elsewhere in the galaxy. Although dust lanes are commonly found associated with nuclear rings (often the leading dust lanes in the bar appear to wrap around a nuclear ring), the ground-based images showed little evidence of dust lanes in ESO 565-11.

BPC also noted a subtle aspect of the light coming from the nuclear ring region: the apparent orientation of the major axis of the starlight in the ring region appears to change smoothly from $H\alpha$ to *B* to *I*. The $H\alpha$ nuclear ring is misaligned with the bar, while the *I*-band isophotes around the nuclear ring are aligned nearly perpendicular to the bar. BPC suggested that this effect is caused by a combination of

dynamics near an inner Lindblad resonance and the occurrence of episodic star formation in the ring. The implication could be that the orbits of stars born in previous bursts in the ring have been changed because the bar has exerted a torque on a misaligned ring. The extreme intrinsic elongation of the ring may be the reason this effect can be seen at all, and *HST* makes it possible to examine it in more detail.

3.2. High-Resolution Imaging and Morphology

Figure 1 shows a montage of the *U*-, *B*-, *V*-, and *I*-band images, rotated so that north is at the top and east is to the left. Especially in the *V* and *I* images, the nuclear ring region appears very much like a spiral. This impression is largely caused by two strong dust lanes that appear to cross into the ring region from the leading edges of the bar. These lanes cannot be traced very far out into the bar region, and they also do not appear to spiral inside the nuclear ring. More details on the dust in the ring region are shown in the *V*–*I* color index map in the bottom left panel of Figure 2. Although there is a clear dust pattern in the center and inside the ring, these patterns do not really seem connected with the main lanes.

The stellar associations appear to trace a true ring rather than a spiral. This is seen best in the *U*-band image in Figure 1 and in the *U*–*B* color index map in Figure 2. The associations in the ring do not preferentially lie on the inner or outer edges of the dust lanes but are found on either side. Only a few of the bright associations are seen in the UV image (Fig. 3).

It is clear from these images that most of the nuclear ring “knots” seen in ground-based images are not single associations. Many of the knots are pairs or even groups of associations. In order to directly connect what is seen in the PC images to the objects seen from the ground, we show in Figures 4 and 5 the locations of the apparent centroids of the ground-based objects. For the *B* band, the PC image was convolved with a Gaussian having $\sigma = 0''.7$ to match the seeing of the “TI #3” CCD image published by Buta & Crocker (1991). Figure 4 shows the *B*-band image with overlying circles showing the locations of the blue knots that appeared in the ground-based images. A few of the objects are nearly centered within the circles, but mostly the knots previously seen are groups of several well-separated objects.

The locations of the $H\text{ II}$ regions compiled by BPC provide a slightly different picture. BPC identified 10 major $H\text{ II}$ regions in the ring and three probable fainter ones. Also, two $H\text{ II}$ regions were found just off the northeast and southwest ends of the ring in the inner parts of the bar. Figure 5 shows the locations of these objects in the *B*-band PC image based on the position offsets compiled in Table 7 of BPC. First, BPC $H\text{ II}$ regions 11, 12, and 14, which were only suspected, are verified to be connected with existing associations in the ring. Second, the $H\text{ II}$ regions mostly favor individual associations, rather than groups of associations, but a few, such as BPC Nos. 5, 10, and possibly even 1, may be groups. Note that it was not possible to obtain a direct $H\alpha$ map of the nuclear ring with *HST*, as a result of the unfavorable redshift.

Images of the core region of ESO 565-11 in *U*, *B*, *V*, and *I* filters is shown in Figure 6. Definite structure is found in this region. In the *U* band, a small oval is seen that persists with an increasing minor-to-major axis ratio from *U* to *I*. It

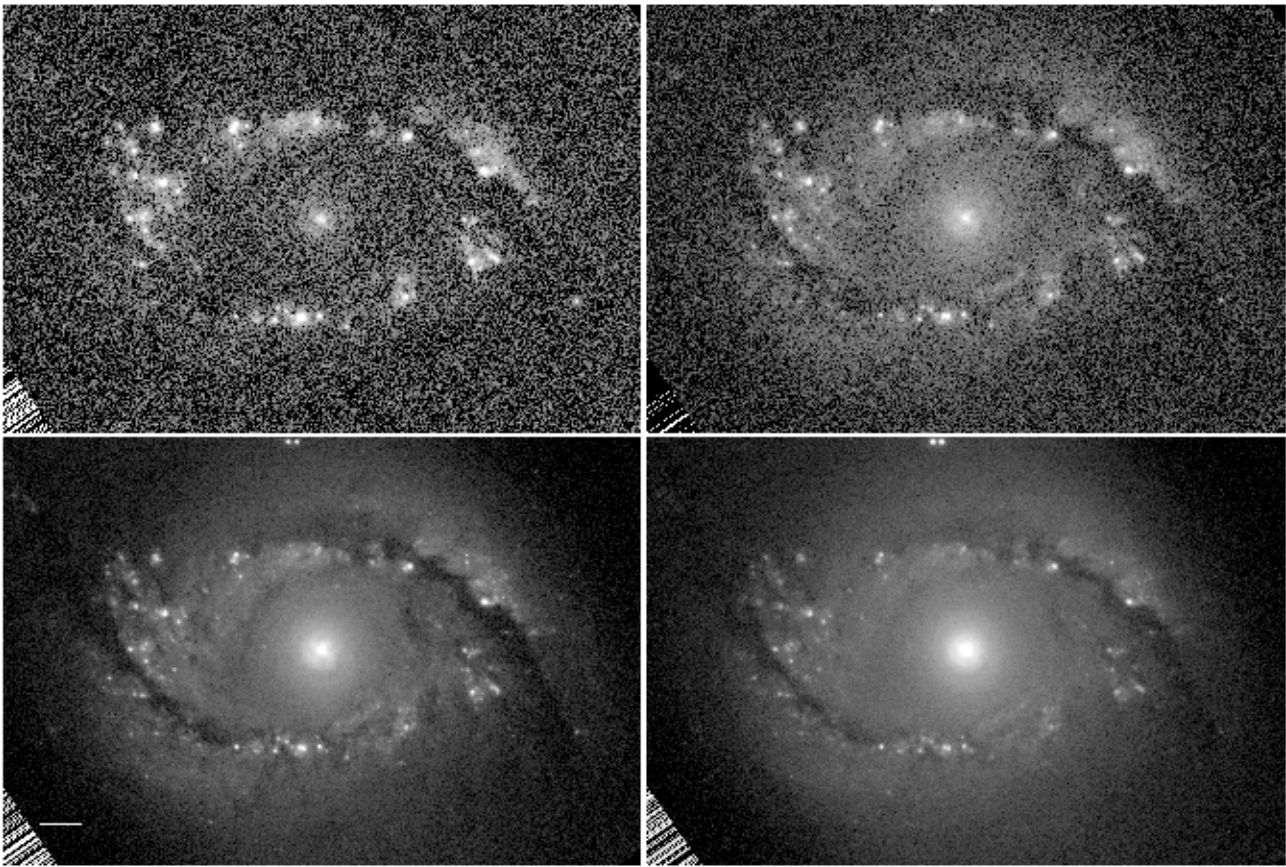


FIG. 1.—PC images of ESO 565-11: *U* band (top left); *B* band (top right); *V* band (bottom left); *I* band (bottom right). The scale bar at lower left is 2" in length, and the field covered by each frame is $30'.3 \times 20'.3$. North is at the top and east is to the left.

is not clear whether this feature could be considered to be a “microbar.” There is no evidence for a normal secondary bar inside the ring, even in *I*. More interesting than the microbar is the weak X-shaped pattern in the inner $0''.5$ radius. The pattern may be an artifact of dust; this is discussed further in § 5.5.

3.3. Near-Infrared Morphology

Our *H*-band image of ESO 565-11 is shown in Figure 7. Most noteworthy in this image is how the nuclear ring is still visible as a highly elongated, knotty feature. This characteristic has been noted in near-infrared images and color index maps of other nuclear rings (Knapen 1996; Friedli et al. 1996). The knots can be related to distinct young clusters in the ring, and their presence at *H* suggests that young red supergiants impact the near-infrared morphology. Also noteworthy in Figure 7 is the “ansae” nature of the bar, meaning that the ends are defined by two elongated enhancements. Both the inner and the outer pseudorings are detected as spiral patterns at *H*.

4. THE RING CLUSTERS

It is interesting now to examine at greater image scale the apparent star-forming complexes in the nuclear ring. Although the ring complexes are brighter in *U* and *B* relative to the background starlight, we illustrate the complexes in *V* because the total exposure in this filter has the best signal-to-noise ratio. Since the H II regions line the ring fairly regularly, we illustrate in Figures 8a–8d $5'' \times 5''$ boxes

centered on the 15 positions circled in Figure 5. These close-ups reveal how most of the ground-based knots are convolutions of several distinct clusters with the seeing disk. The regions around the ring major axis are rich in resolved objects.

The construction of a catalog of the clusters and other stellar objects in the central area (including those in areas outside and inside the ring) was carried out in three steps. First, we ran the routine DAOFIND (part of the DAOPHOT package in IRAF) on the *V*-band image to obtain a first-pass list of objects. The *V*-band image was used because all of the stellar objects are best seen on this image even though many are blue. DAOFIND successfully found most of the clusters. However, it also found many spurious objects and missed finding some clusters. We were able to remove most of the spurious objects in the ring region by comparing the *B* and *V* or *V* and *I* images and making sure that objects are generally seen in both images. The missed objects were added to the catalog using IRAF routine TVMARK. In the third step, the *V*-band image was run through DAOPHOT routine ALLSTAR using a preliminary point-spread function (PSF) (see below), and the object-subtracted image was inspected for any faint companions to bright objects that were missed in the first two steps. These were then added to the coordinate list using TVMARK. The final catalog of 780 objects was based on a second pass of PSF fitting to the *V*-band image, allowing the centers of the objects to be adjusted to improve the fits.

Although the registration of the images in different filters is very good, we still had to apply small corrections to the

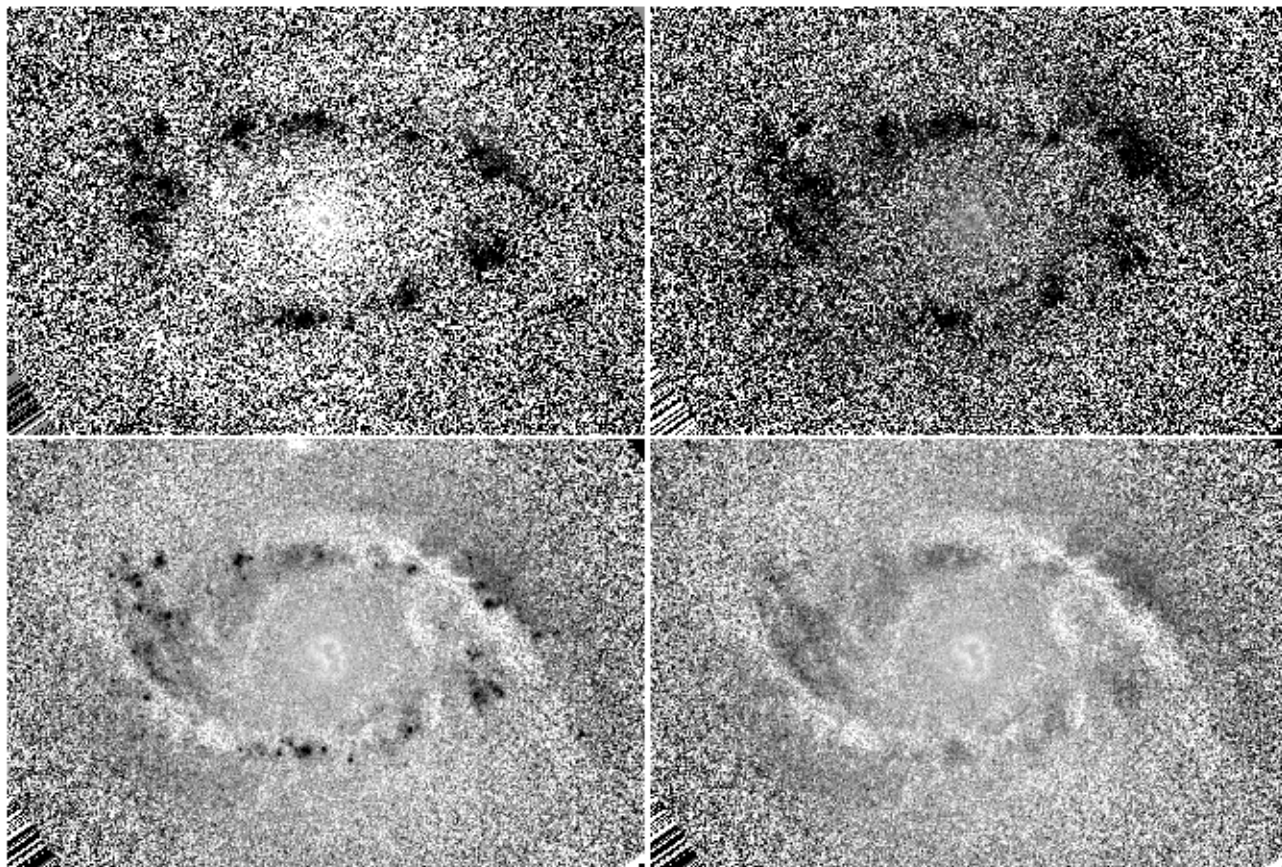


FIG. 2.—PC color index maps (dark = blue, light = red) of ESO 565-11: $U-B$ (top left); $B-V$ (top right); $V-I$ with clusters (bottom left); $V-I$ after removal of clusters (bottom right). Image scale and orientation are the same as for Fig. 1. The field covered by each frame is $30''.3 \times 20''.3$. North is at the top and east is to the left.

V -band position catalog before using it with the other filters. In order to ensure that the same relative coordinates were being used for all filters, we derived linear offsets in pixels between the V -band positions of 25–40 objects in the ring and their positions in the other filters. These offsets were used to produce corrected position catalogs for the other filters. Recentering was not allowed in the other passbands, since noise could allow positions to shift significantly.

Even at the resolution of the PC, there is considerable overlapping of the PSFs of many of the ring clusters. Some are relatively isolated, however. As a result, we have used a combination of PSF fitting and aperture photometry to estimate the magnitudes and color indexes of the objects. The DAOPHOT package (Stetson 1987) in IRAF was used for PSF fitting, while the APPHOT package was used for aperture photometry.

Unfortunately, for PSF fitting there are only two clear foreground stars on all of our images: a close pair of stars of similar magnitude due north of center that are most prominent in I . The close proximity of these stars together in the field and their extreme faintness in U and B (and complete invisibility in the UV image) precluded our use of them to directly define the PSF. Initially, we used instead the TinyTim software package (Krist 1995) to generate artificial PSFs for the filters and dates of our observations. Since the PSF may depend slightly on position within the field, we computed artificial PSFs at 15 different locations around the ring area to allow us to map any variability with posi-

tion. The characterization of the PSF was computed using DAOPHOT routine PSF, with the parameter “varorder” set to 0, 1, or 2 to test the significance of any variations. Little variation was found over the region of interest. However, we found that TinyTim PSFs did not represent the cluster PSFs very well. The full width at half-maximum (FWHM) of the TinyTim PSFs was 1.35 pixels versus 1.75–2.0 pixels for the cluster images. The difference may indicate slight resolution of the clusters compared with a true point source.

To do better, we created an initial PSF for each filter image using the few most isolated bright clusters with a fit radius of 2 pixels, a PSF radius of 6 pixels, and sky taken between a 7 and 17 pixel radius. This PSF was then used with DAOPHOT routine ALLSTAR with an initial magnitude file to compute fitted magnitudes. The ALLSTAR output file was then used to remove faint companions from a few other clusters to increase the number of PSF objects, and a revised initial PSF was constructed. With the revised initial PSF, ALLSTAR was run again to produce a cluster-subtracted image. This is illustrated for the V band in the top right panel of Figure 9.

In the next step, we flattened the background under the clusters by median-smoothing the cluster-subtracted images using a 5×5 pixel filter and subtracting these images from the original ones. This was useful because most of the ring clusters lie on complex backgrounds with dust lanes and other irregularities. The median smoothing removed well any small residuals left from the PSF-fitting process (see

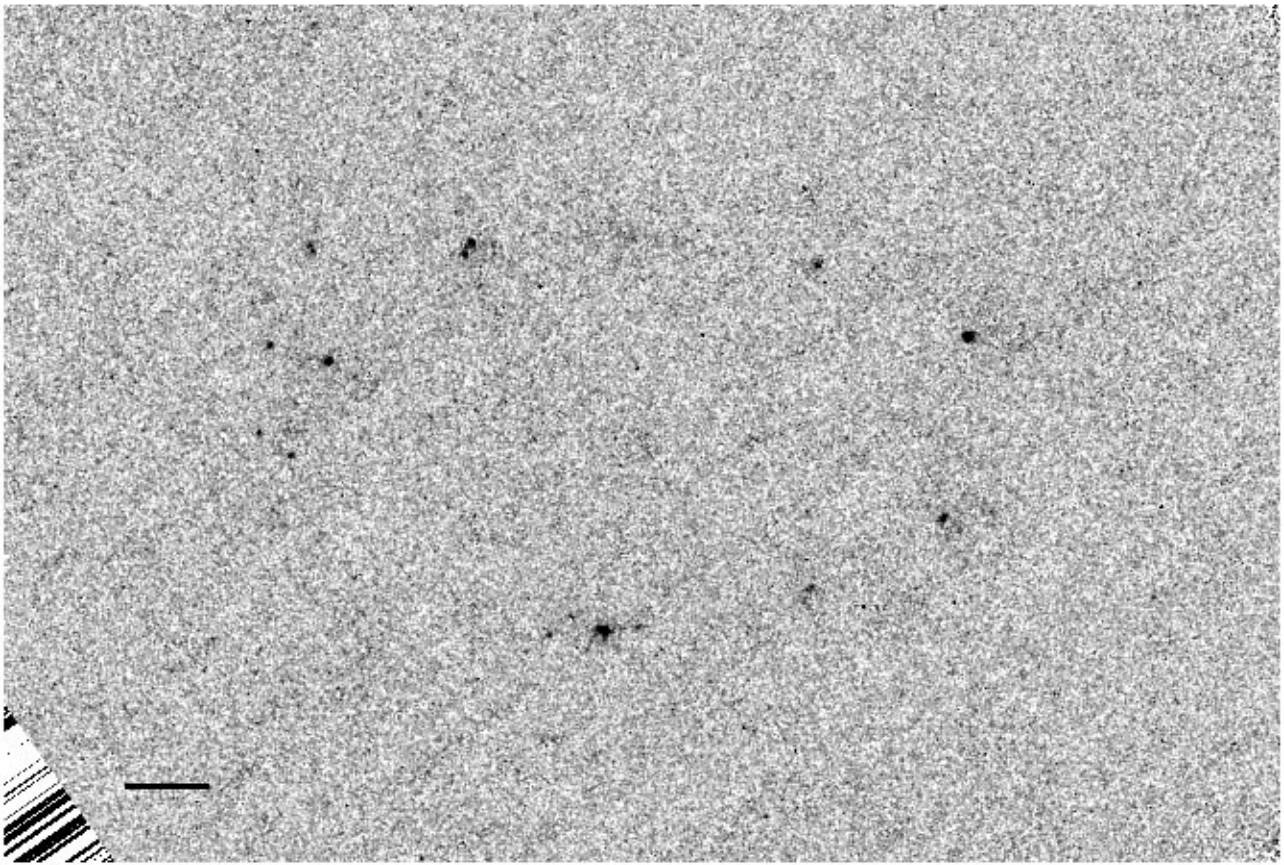


FIG. 3.—UV image (filter F255W) of the nuclear ring of ESO 565-11. The scale bar at lower left is 2" in length, and the field covered by the frame is $30'.3 \times 20'.3$. North is at the top and east is to the left.

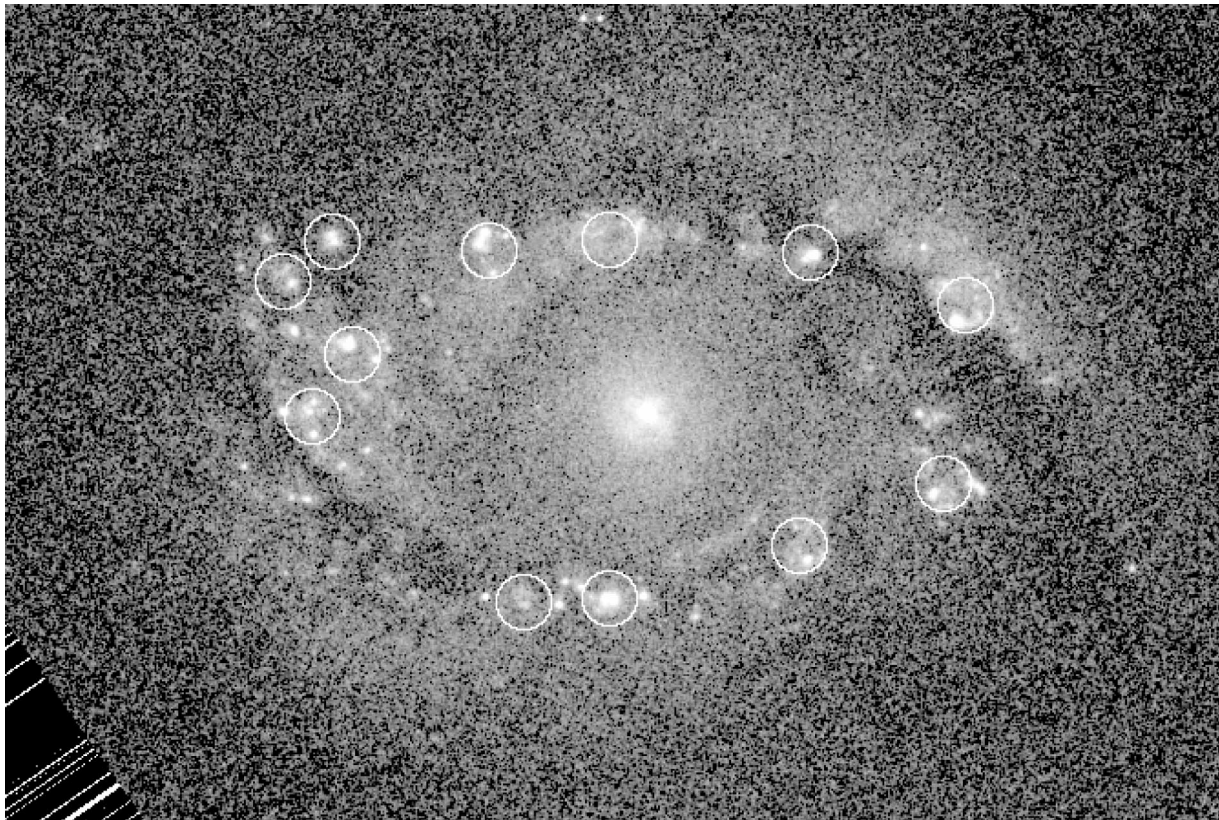


FIG. 4.—*B*-band PC image of the nuclear ring. The superposed circles show the locations of "knots" seen in the ground-based images published by Buta & Crocker (1991). The field covered by the frame is $30'.3 \times 20'.3$. North is at the top and east is to the left.

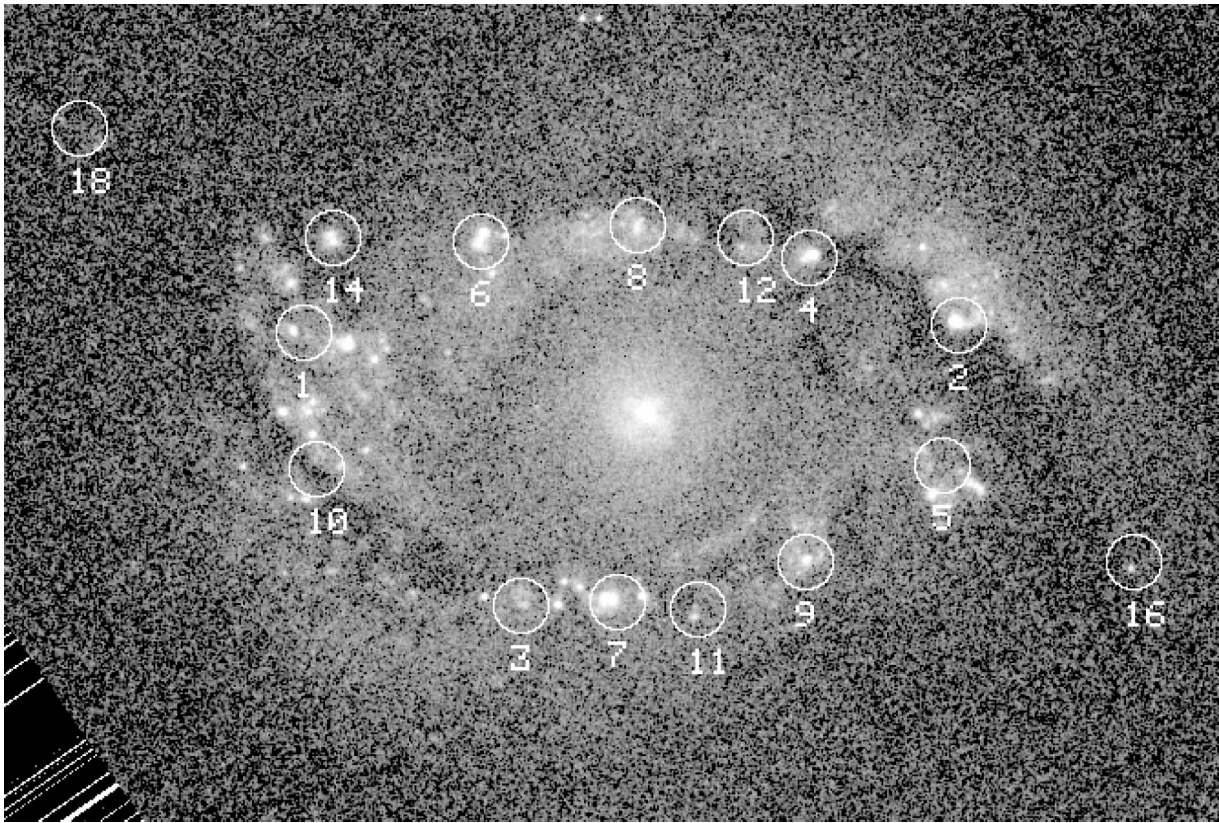


FIG. 5.—*B*-band PC image of the nuclear ring. The superposed circles show the locations of H II regions compiled by BPC from a ground-based image. The field covered by the frame is $30''.3 \times 20''.3$. North is at the top and east is to the left.

Fig. 9, *bottom left*), and the choice of box size effectively eliminated almost all trace of the background (see Fig. 9, *bottom right*). For a few of the brighter clusters, the ALLSTAR residuals were sometimes removed using IRAF routine IMEDIT, since median smoothing did not always eliminate the traces of these residuals. Use of a much larger median-smoothing box size could have eliminated some of these residuals better, but larger box sizes did not flatten the backgrounds very effectively. The 5×5 pixel box size proved most effective. After flattening the background, we added back a mean background level so that the errors in our magnitudes could be computed reliably. Then the same steps in obtaining a PSF for the unflattened images were carried out on the flattened images, except that the sky levels were fixed to a constant on each filter. Up to 12 clusters were used to get the final PSFs, depending on how effectively ALLSTAR could remove faint companions.

The procedure for the UV image differed from the above mainly in that it was not necessary to flatten the background with median smoothing and that only one cluster could be used to define the PSF. Only 21 clusters are clearly detected in the cosmic-ray-cleaned image, and there is no trace of the background galaxy light. Otherwise, the rest of the procedure was the same as for the other images.

We derived two sets of natural magnitudes for our final analysis. First, ALLSTAR was run on the image for each filter with the appropriate PSF and background noise level. Since ALLSTAR needs an initial input list of magnitudes, we ran APPHOT routine PHOT first on each image using an aperture radius of 2 pixels. Judging from the quality of the object-subtracted images produced by ALLSTAR, we believe the ALLSTAR magnitudes to be as good as can be

obtained by the procedure. However, given the difficulty of defining the PSFs very accurately on any of the images, owing to a lack of isolated and relatively bright field objects, we believe that aperture photometry is superior for those objects that are either relatively isolated or that can be cleaned well of fainter close companions. For this reason, we selected a subset of 49 bright objects and used the ALLSTAR fits to subtract all but these 49 objects from the original images. We also identified in the *V*-band cluster catalog a set of 197 additional (mostly very faint) objects that had no companions within a 6 pixel radius and that therefore could be considered isolated enough for aperture photometry. For all of these objects, we used PHOT to compute the magnitudes within an aperture radius of 2 pixels, and this photometry was then compared with ALLSTAR photometry for the same objects. In general, there was very good relative agreement between the ALLSTAR magnitudes and the PHOT magnitudes for these objects, and the comparisons were used to compute weighted mean offsets in magnitudes between PHOT and ALLSTAR estimates. The ALLSTAR magnitudes were then reduced to the system of the $r = 2$ pixel PHOT magnitudes so that all final *total* magnitudes could be obtained by applying the same aperture corrections.

At this point, we made several other small but important instrumental corrections to the magnitudes. Corrections for geometric distortion (see Holtzman et al. 1995b) were made by obtaining the publicly available distortion image f1k1552bu and extracting the PC distortion correction (generally very close to unity) at the position of each object. The corrections for charge transfer efficiency (CTE; see Holtzman et al. 1995a) were made using equations (1), (2a),

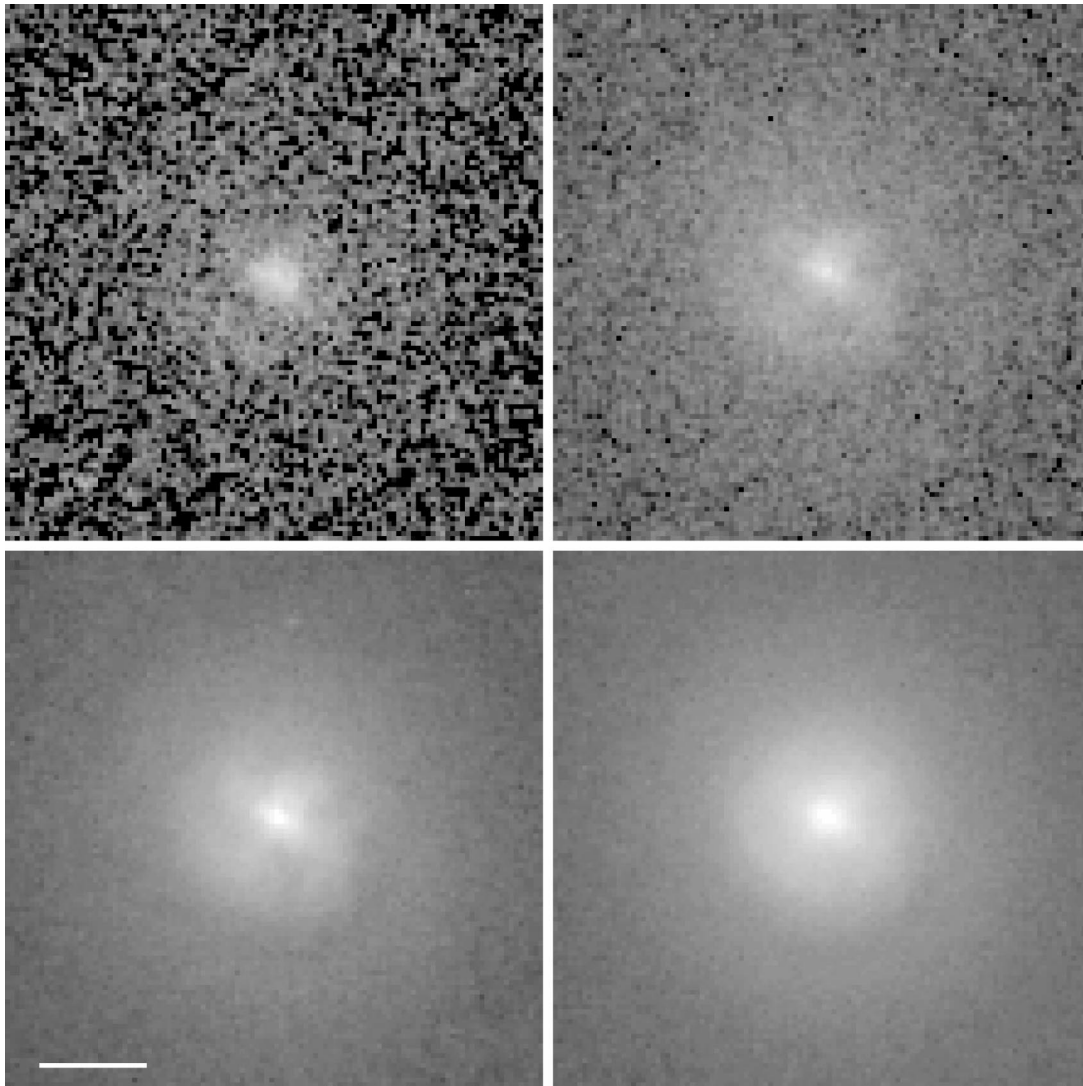


FIG. 6.—PC images of the core region of ESO 565-11: *U* band (top left); *B* band (top right); *V* band (bottom left); *I* band (bottom right). The scale bar at lower left is 1" in length, and each frame is $5'' \times 5''$ in area. North is at the top and east is to the left.

and (3a) from Whitmore & Heyer (1997). These allow for both x and y CTEs and use the mean counts on the chip, which we derived using the IRAF routine IMSTAT over the region from pixels [100:700, 100:700]. Corrections for contamination loss (see also Holtzman et al. 1995a) were made using the standard procedure (see WFPC2 Data Analysis Tutorial, version 2.0, 1998 and Tables 28.2 and 28.3 of the *HST* Data Handbook).

Another potentially important correction concerns the red leaks in the F255W and F336W filters. Table 3.13 of the *HST* Data Handbook provides flux percentages of the leaks as a function of stellar spectral class. Using basic data from Lang (1992), we computed a polynomial representation of the red leak percentages as a function of $B - V$ for each filter and used these polynomials to make corrections according to the observed $B - V$ colors measured for ring clusters. Fortunately, for most of the stellar objects in the ring, these corrections are less than 1%.

The next step in the analysis was to determine the aperture corrections. Although encircled energy (or “growth”) curves of stellar objects are provided for all of our filters by Holtzman et al. (1995b), we decided to derive the appropri-

ate curves from our images directly to check whether the published curves are in fact applicable to our data. For this purpose, we selected a number of relatively bright clusters ranging from one cluster in the UV filter to nine to 12 clusters in the *UBVI* filters, and then cleaned their areas of fainter companions (using ALLSTAR fits and, if necessary, IMEDIT) so that no contaminating objects lay within 15 pixels radius of any of them. Then PHOT was used to compute magnitudes of these objects in 15 apertures ranging from 1 to 15 pixels in radius. The growth curves were compared between each object in the range 2 to 9 pixels to derive mean offsets in magnitudes between the objects and a reference object. Then the reduced magnitudes were averaged (where relevant) at each radius to produce a higher precision mean growth curve. The resulting curves are shown in Figure 10. For comparison, we also show the curves from Holtzman et al. (1995b). In all filters, the derived curves depart slightly from the published ones in the sense that the clusters are slightly more extended. This is consistent with what was found in the PSF analysis, and thus we believe we should use our derived growth curves rather than the Holtzman et al. curves. Fol-

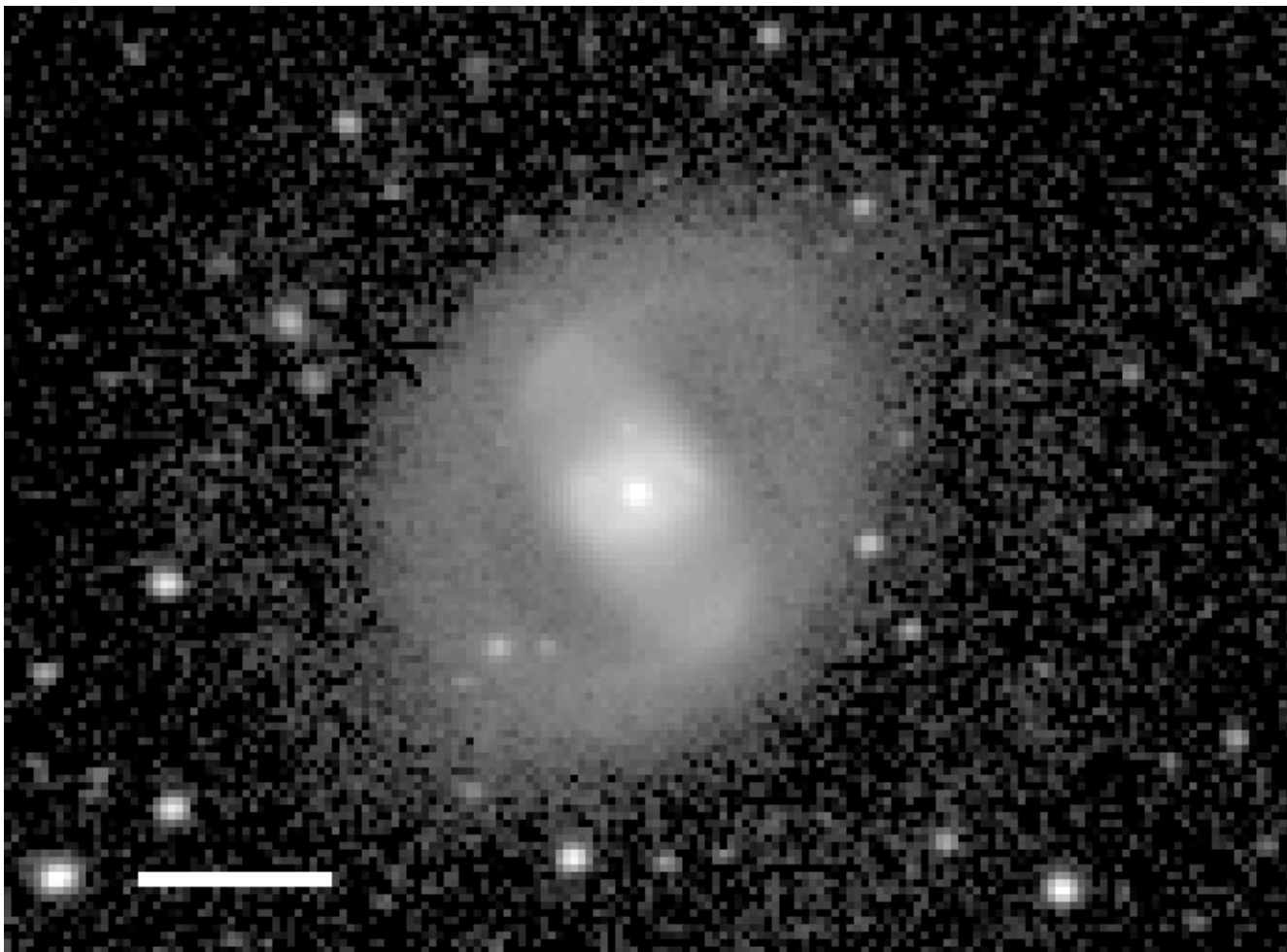


FIG. 7.—Near-infrared (H band) image of ESO 565-11. The image is logarithmic and in units of mag arcsec^{-2} , ranging from 15.0 to 24.0 mag arcsec^{-2} . North is at the top and east is to the left. The scale bar at lower left is 30" in length.

lowing Holtzman et al. (1995a), we apply aperture corrections in order to get magnitudes within a reference 0".5 (11 pixel) radius aperture. From our mean growth curves, the corrections needed for a 2 pixel radius magnitude are 0.575 ± 0.028 mag for F255W, 0.518 ± 0.021 mag for F336W, 0.518 ± 0.025 mag for F439W, 0.462 ± 0.013 mag for F555W, and 0.659 ± 0.016 mag for F814W. The $UBVI$ values compare favorably with those derived in a similar manner by Miller et al. (1997) for clusters in NGC 7252, a galaxy at a similar distance.

The final step in the analysis is the conversion of these corrected natural magnitudes into standard magnitudes in the $UBVI$ photometric system. For this purpose, we used equation (8) and Table 7 of Holtzman et al. (1995a) for $UBVI$ transformations and Table 9 from the same paper for the zero point of the F255W filter. However, before applying these transformations and zero points we made a correction to the natural magnitudes for Galactic extinction using the B -band extinction of 0.08 mag provided in the RC3 (de Vaucouleurs et al. 1991), a ratio of total to selective extinction of 3.1, and Table 12a of Holtzman et al. (1995a), which assumes most of the clusters have an early-type stellar spectrum. As noted by Holtzman et al. (1995a), correcting the natural magnitudes rather than the transformed magnitudes is essential because of the different effective wavelengths of the WFPC2 filters compared with standard

$UBVI$ filters. It is not possible for us to make a preliminary correction for internal extinction because we do not know $E(B-V)$ for any of the individual clusters, and a single average value may not be appropriate. Table 12a of Holtzman et al. (1995a) does not list extinction parameters for the filter F255W. In this case, we derived the Galactic extinction correction using equations (4a) and (4b) of Cardelli, Clayton, & Mathis (1989) with an inverse wavelength of $x = 3.864 \mu\text{m}^{-1}$. This gave $A_{UV}/A_V = 2.173$.

Table 1⁵ summarizes the photometry for 780 objects, of which 117, mostly fainter than $V_c = 25.0$, are listed only with a V magnitude. The numbering system for the objects is arbitrary, and in order to prevent confusion, we have not changed it. Columns (2) and (3) of Table 1 give offsets of the clusters from the nucleus in arcseconds, such that Δx is positive to the west and negative to the east and Δy is positive to the north and negative to the south. Columns (4)–(7) give the magnitudes and colors of the clusters, while columns (8)–(11) give the photometric errors in these parameters. Table 2 summarizes the UV magnitudes m_{F255W} and colors $m_{F255W} - V$ for 21 clusters. The errors in

⁵ The printed version of this paper lists in Table 1 only the 39 clusters having $V_c \leq 22.0$. The electronic version provides the whole list of 780 objects.

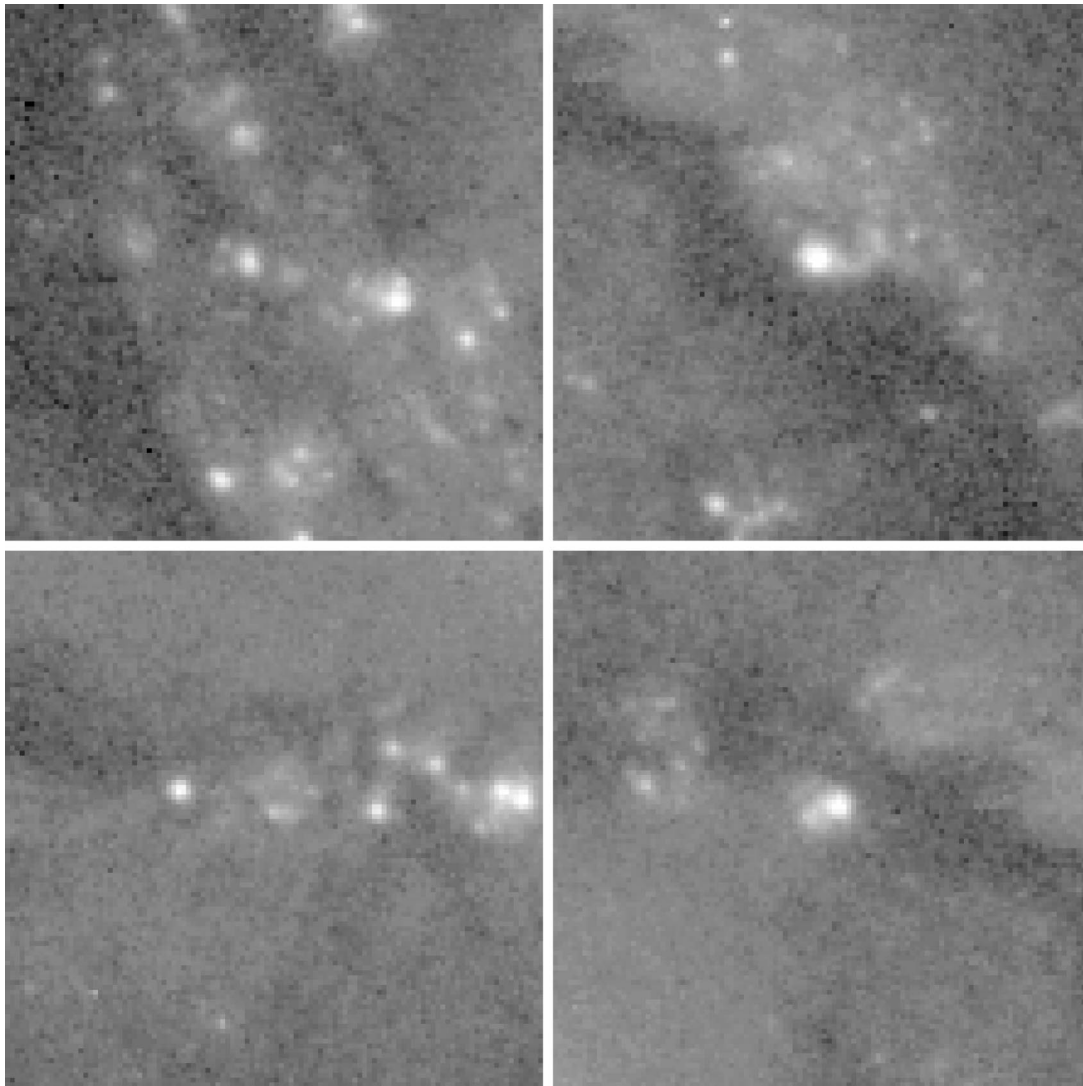


FIG. 8a

FIG. 8.—Enlarged illustrations of $5'' \times 5''$ areas around the 15 labeled H α -emitting regions in Fig. 5, in logarithmic units based on filter F555W. Four sets of images are shown, with identities as follows. *Upper left frames:* 1, 5, 9, 14; *upper right frames:* 2, 6, 10, 16; *lower left frames:* 3, 7, 11, 18; *lower right frames:* 4, 8, 12. North is at the top and east is to the left.

the listed parameters include the statistical and fitting errors from PHOT and ALLSTAR, the uncertainties in the aperture corrections, and the uncertainties connected with the transformations to the standard systems.

As a check on the zero points of the transformations, we have used the calibrated ground-based CCD images of ESO 565-11 obtained by Buta & Crocker (1991). These images, which were obtained with a Texas Instruments (TI) 800×800 pixel CCD operated in a 2×2 binning mode, have better seeing than those used mainly by BPC and have a good standard-star calibration. However, the images were only obtained in B , V , and I . For the comparison, we degraded the resolution of the PC images to those of the ground-based TI images, which have a scale of $0''.547$ pixel $^{-1}$ and a mean stellar FWHM of $1''.8$. The galaxy was then integrated on the TI and degraded PC images in 22 apertures centered on the nucleus ranging from $2''$ to $23''$ in diameter. An important problem in this comparison is how to correct for any “sky” background in the PC images. We cannot determine this directly from our images. Instead, we have used Tables 6.1, 6.2, and 6.3 of the WFPC2 Instrument

Handbook, version 3.0, to make a reasonable judgment of this background correction for each filter. The ecliptic latitude of ESO 565-11 is $\approx 30^\circ$, so we take the sky background to be 22.9 mag arcsec $^{-2}$ in the V band. Using filter zero points on the Vegamag system from Table 1 of Whitmore (1995), the values of AB_v for the sky interpolated at the mean wavelengths of the filters from Table 6.1 of the Instrument Handbook, and allowing for exposure time, we estimated contributions of 0.0066, 0.082, 0.435, and 0.331 counts in data numbers for our F336W, F439W, F555W, and F814W images, respectively.

The integrated fluxes from the TI images were transformed to the standard systems based on 13 standards from Graham (1982) and Landolt (1992). The relations were derived using the PHOTCAL package in IRAF and were linear in color term and air mass for each filter. The integrated fluxes from the degraded PC images were transformed to the standard systems again using equation (8) and Table 7 of Holtzman et al. (1995a), with one modification: we added 0.1 mag to the zero points of Holtzman et al. (as recommended by those authors) to correct to infinite

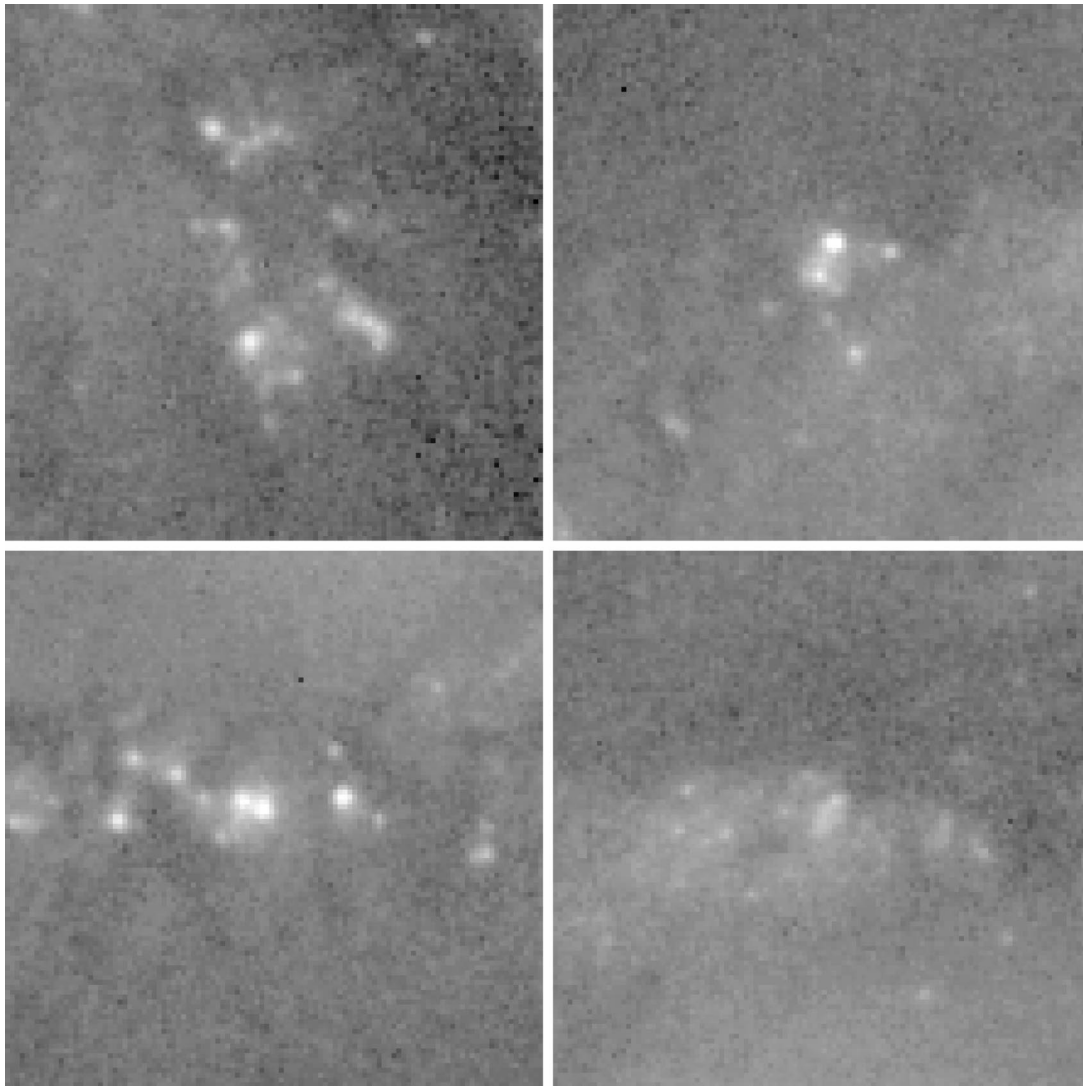


FIG. 8b

aperture since the fluxes were integrated in apertures much larger than $0''.5$. The resulting comparisons for the 22 apertures were $\langle B_{\text{TI}} - B_{\text{PC}} \rangle = -0.045 \pm 0.005$ (s.d.), $\langle V_{\text{TI}} - V_{\text{PC}} \rangle = +0.008 \pm 0.006$ (s.d.), and $\langle I_{\text{TI}} - I_{\text{PC}} \rangle = +0.040 \pm 0.012$ (s.d.). The standard deviations are very small, implying that the inferred background corrections are probably reasonable. The zero-point differences are less than ± 0.05 mag, which is quite satisfactory. In the U band, the only comparison we can make is with a photoelectric measurement made with a $19''.9$ aperture published by Buta & Crocker (1992). Following the same procedure as above, we obtain $U_{\text{pe}} - U_{\text{PC}} = +0.238$ with an uncertainty of at least ± 0.05 mag. This is poor agreement but is similar to the difference, 0.16 mag, obtained by Miller et al. (1997) when they made a similar comparison. This large disagreement weakens our use of the $U-B$ color index, but as shown in § 5, we find reasonable agreement between our measured $U-B$ colors of the brighter ring clusters and available evolutionary synthesis models.

5. DATA ANALYSIS

5.1. Two-Color Data

Our goal in this section is to judge the ages, metallicities, and possible reddenings of the observed ring clusters. We

also attempt to identify whether a population of older, redder clusters from a previous burst of star formation may still exist in the ring region. For these purposes, we use two-color plots of the Galactic extinction-corrected colors ($m_{\text{F255W}} - V$) $_c$, ($U - B$) $_c$, ($B - V$) $_c$, and ($V - I$) $_c$ of the clusters. Publicly available evolutionary synthesis models can be used to judge the evolutionary status of the clusters. For our comparisons, we use the models of G. Bruzual & S. Charlot (hereafter BC96) as compiled by Lejeune, Cuisinier, & Geisler (1996) and described by Leitherer et al. (1996). These models follow the evolution of spectra and colors of model star clusters using isochrone synthesis (Bruzual & Charlot 1993). The models cover a range of metallicities, $Z = 0.0004, 0.004, 0.008, 0.02, 0.05, \text{ and } 0.10$, and use two initial mass functions (IMFs): Salpeter (1955) and Scalo (1986). We compared our clusters with the evolutionary curves for both IMFs and all of the available metallicities for all clusters having $V_c \leq 22.0$, i.e., the brightest clusters, and can safely rule out metallicities $Z < 0.02$ and $Z > 0.05$. Here we only make comparisons with the $Z = 0.02$ (solar) and $Z = 0.05$ cases. Little difference is seen between the Salpeter and Scalo IMFs for these metallicities, so we also illustrate only the comparisons with the Salpeter IMF models.

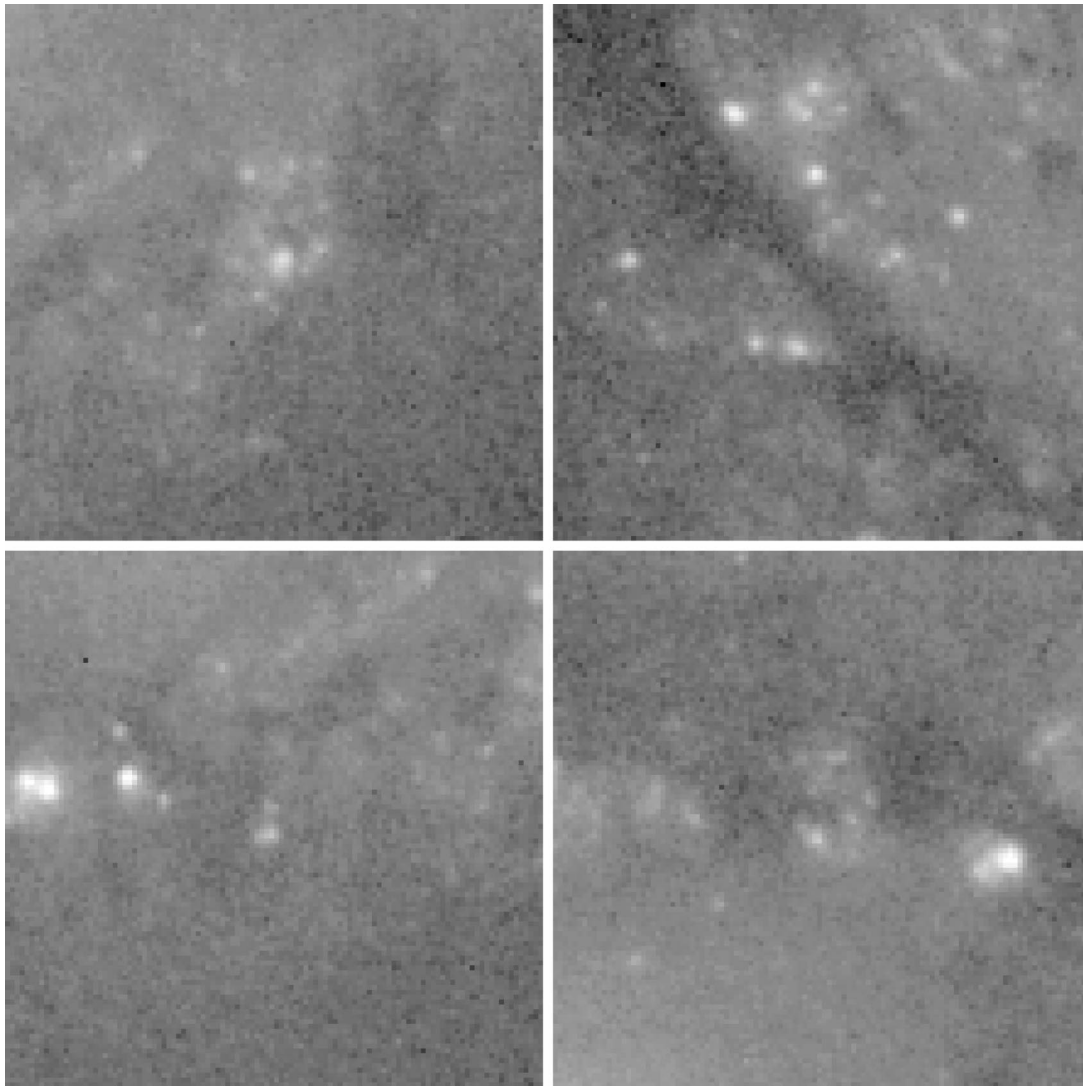


FIG. 8c

BC96 do not provide models of the $m_{F255W} - V$ color index we have measured. Instead, they computed colors $2200 - V$ and $2700 - V$ for UV wavelengths that bracket F255W. For the comparison, we simply linearly interpolated an approximate $m_{F255W} - V$ color index using $\lambda = 2588 \text{ \AA}$ for the F255W filter (Holtzman et al. 1995a).

For display we divide the clusters according to corrected V magnitude, since the errors in the color indexes increase fairly rapidly with increasing V magnitude. Figures 11a–11c show the two-color plots for Galactic extinction-corrected magnitude $V_c \leq 22.0$, $22.0 < V_c \leq 23.0$, and $23.0 < V_c \leq 24.0$, respectively. For Figures 11a and 11b, there is also the requirement that the clusters have a measured $U - B$, while Figure 11c shows only $(B - V, V - I)$ plots in order to determine if there is a population of either redder or heavily reddened clusters. The dotted arrow in each figure indicates the reddening line for an extinction A_V of 1.0 mag. The brighter clusters in Figure 11a straddle the upper parts of the BC96 models well for both $Z = 0.02$ and $Z = 0.05$. The crosses on these parts of the evolutionary curves are separated by 1 Myr and range from 1 to 10 Myr. The first noteworthy result from these comparisons is how many of the clusters in Figure 11a lie significantly above the BC96

curves for solar metallicity. While we cannot rule out completely a systematic zero-point error in $U - B$, the $(B - V, V - I)$ comparison clearly favors the $Z = 0.05$ model: none of the brightest clusters lies significantly above the upper part of the curve for this model, and many scatter below it in the sense of the reddening vector. The tentative implication is that the clusters may be metal-rich compared with the Sun and that several of the brightest clusters are significantly reddened.

The second noteworthy result from Figure 11a is how eight clusters do not depart significantly from the upper part of the $Z = 0.05$ BC96 model in the $(B - V, V - I)$ plot, implying that they may be little reddened. In these cases we can directly read the ages of the clusters from their location on the evolutionary curve. These eight clusters appear to range from 4.4 to 5.7 Myr in age, indicating a possibly significant spread in ages of the brightest clusters by more than 1 Myr. Several of the reddened clusters could be younger. The age range could be larger since the model curve is ambiguous for ages more than about 5.4 Myr, where the loop occurs. It would not be unexpected that the brightest clusters would be among the youngest.

The clusters in Figure 11b show more scatter than those

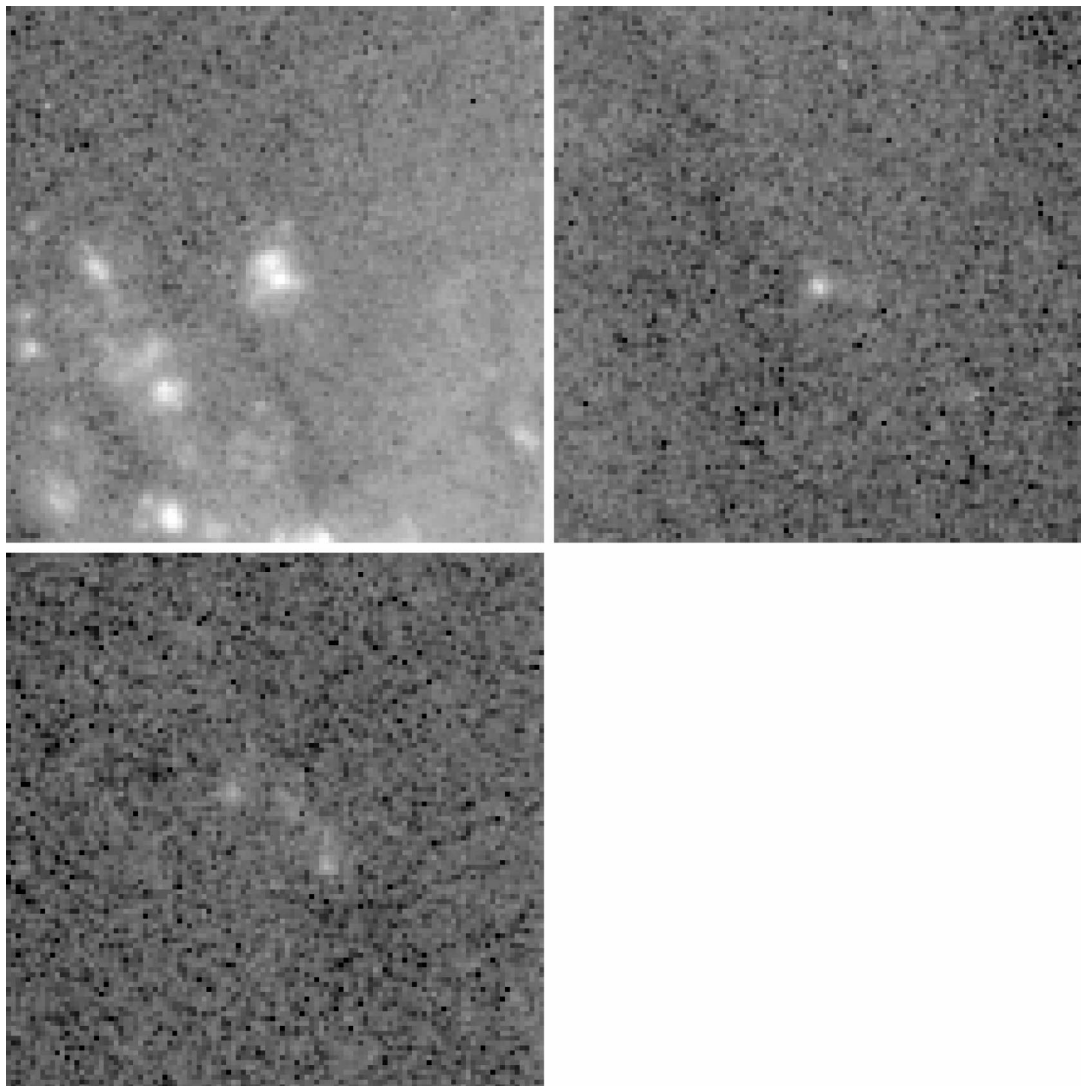


FIG. 8d

in Figure 11a, but the points straddle the upper parts of the model curves in a similar manner. Only three clusters brighter than $V = 23.0$ have $(V-I)_c > 0.70$. Virtually all of the clusters in this magnitude range could be reddened young clusters rather than a mixture of young and old clusters. A more telling view is provided by Figure 11c, where clusters lacking a measurable $U-B$ are included. Only seven objects in this plot have $(V-I)_c \geq 1.0$. These objects, Nos. 33, 91, 122, 489, 524, 549, and 701, lie along or near the ring and are probably clusters; they are too bright and blue to be red supergiants. Since all lie above and to the right of the model curves, it is likely that they are excessively reddened rather than excessively old compared with the other clusters. Only spectroscopy could prove this conclusively.

UV two-color plots are shown in Figure 12. These plots again favor the $Z = 0.05$ BC96 model since it allows the clusters to be slightly reddened. It is obvious that most of the clusters seen in the F255W filter are extinguished by 0.5 mag of visual extinction or less, and so are among the least reddened clusters. The right panels of Figure 12 again suggest that the clusters span an age range of 4–6 Myr.

5.2. Ultraviolet Luminosities and Nuclear Ring Star Formation Rate

Kennicutt (1998) reviews the utility of ultraviolet data for measuring star formation rates in galaxies. Because the integrated light in the UV is dominated by the youngest and most massive stars, the star formation rate (SFR) scales linearly with the UV luminosity. We have integrated the UV flux from the 21 clusters in Table 2 and converted the total to absolute units using equation (10) and Table 11 of Holtzman et al. (1995a). This gave $F_{F255W} = 9.75 \times 10^{-16}$ ergs $s^{-1} cm^{-2} \text{ \AA}^{-1}$. If the distance is 60 Mpc, then the specific luminosity is $L_{F255W} = 4.16 \times 10^{38}$ ergs $s^{-1} \text{ \AA}^{-1}$. This will be a lower limit since we do not know the reddening for each cluster, and Table 11 of Holtzman et al. (1995a) is strictly valid for unreddened sources. Kennicutt (1998) states that for a Salpeter IMF, the composite UV spectrum can be relatively flat in L_ν over the wavelength range 1500–2800 \AA , so we have converted our value of L_{F255W} into L_ν in order to use equation (1) of Kennicutt (1998), which gives the star formation rate for massive stars. The observed total F255W luminosity of ESO 565-11 implies an SFR of $0.13 M_\odot \text{ yr}^{-1}$ (uncorrected for internal

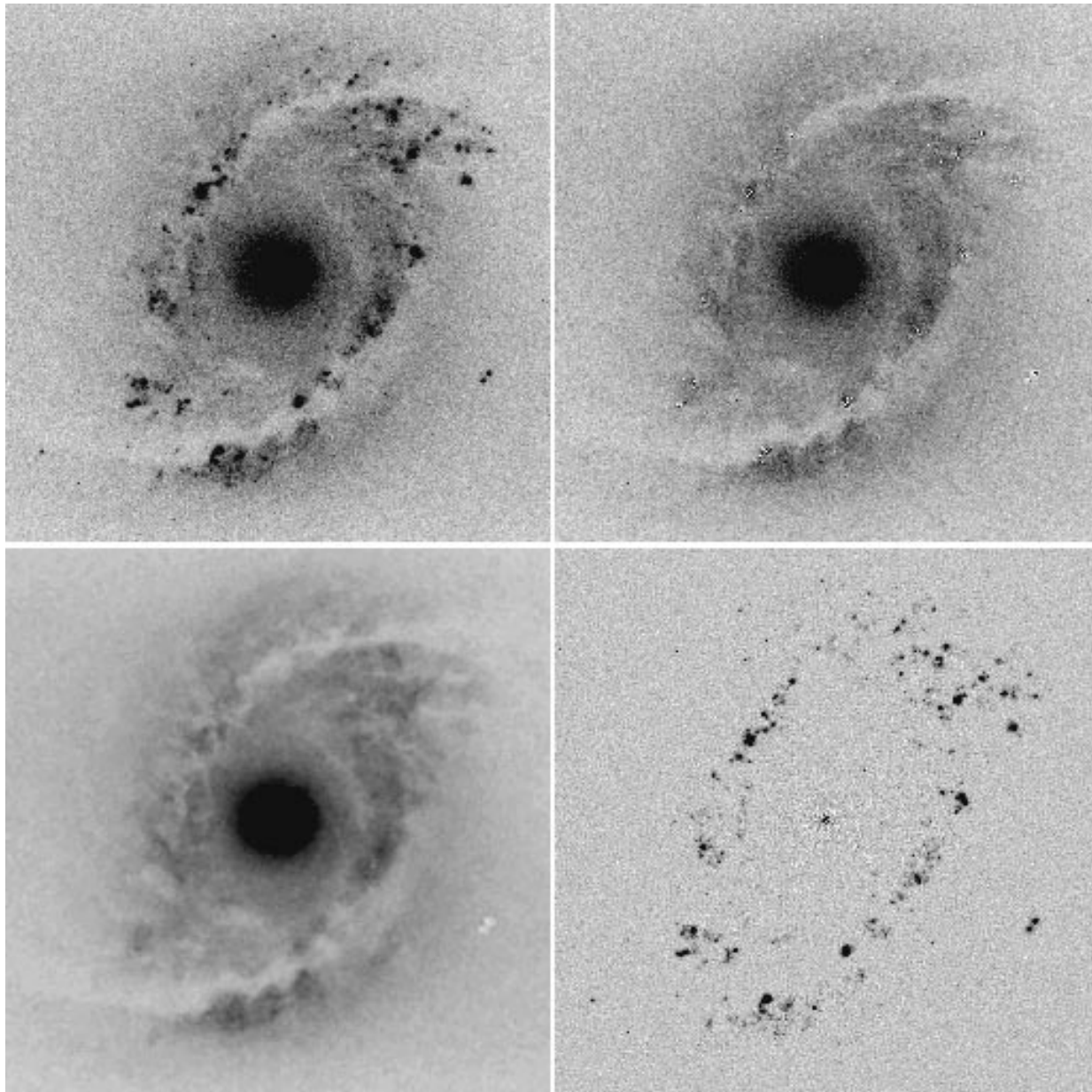


FIG. 9.—Montage of images showing the isolation of the ring clusters from the complex background. *Top left*, original and unrotated F555W image; *top right*, residual F555W image after first-pass removal of 780 clusters and foreground stellar objects, using DAOPHOT routine ALLSTAR; *bottom left*, same image median-smoothed with a 5×5 pixel box to remove small residuals from the ALLSTAR fits; *bottom right*, difference between original F555W image and the median-smoothed image, showing only the ring clusters on a flattened background.

extinction). This estimate is valid only in the continuous star formation approximation, where a galaxy forms stars over a period of 10^8 yr or longer.

5.3. Cluster Luminosity Function

The differential apparent luminosity function of the ring clusters is shown in Figure 13. Although the magnitudes are corrected for Galactic extinction, no correction for internal extinction could be made. A distance modulus of 33.89 has been assumed. The luminosity function immediately shows that the brightest clusters in the ring are “super-star clusters,” a term first applied to the massive clusters seen with *HST* in several starburst and interacting galaxies, and more recently to the luminous clusters seen in other nuclear rings (Barth et al. 1996 and references therein). That the clusters

are compact is shown by the growth curves in Figure 10. From 12 clusters, the mean FWHM is 1.88 pixels in the *V* band. Using a TinyTim PSF, and assuming Gaussian profiles, the corrected dispersion size of the clusters is $R_\sigma = 7$ pc. This compactness suggests that they are young globular clusters.

The luminosity function shows a significant drop-off for $M_V > -8.9$ ($V_c > 25.0$), which we attribute mainly to incompleteness. This assertion was tested by using the cluster-free *V*-band image (Fig. 9, *top right*) after an initial run of ALLSTAR and adding artificial clusters to this image using IRAF routine ADDSTAR. A random number generator was used to randomly position a set of about 450 clusters in 0.25 mag bins along the ring, and then DAOPHOT routine DAOFIND was used to find the arti-

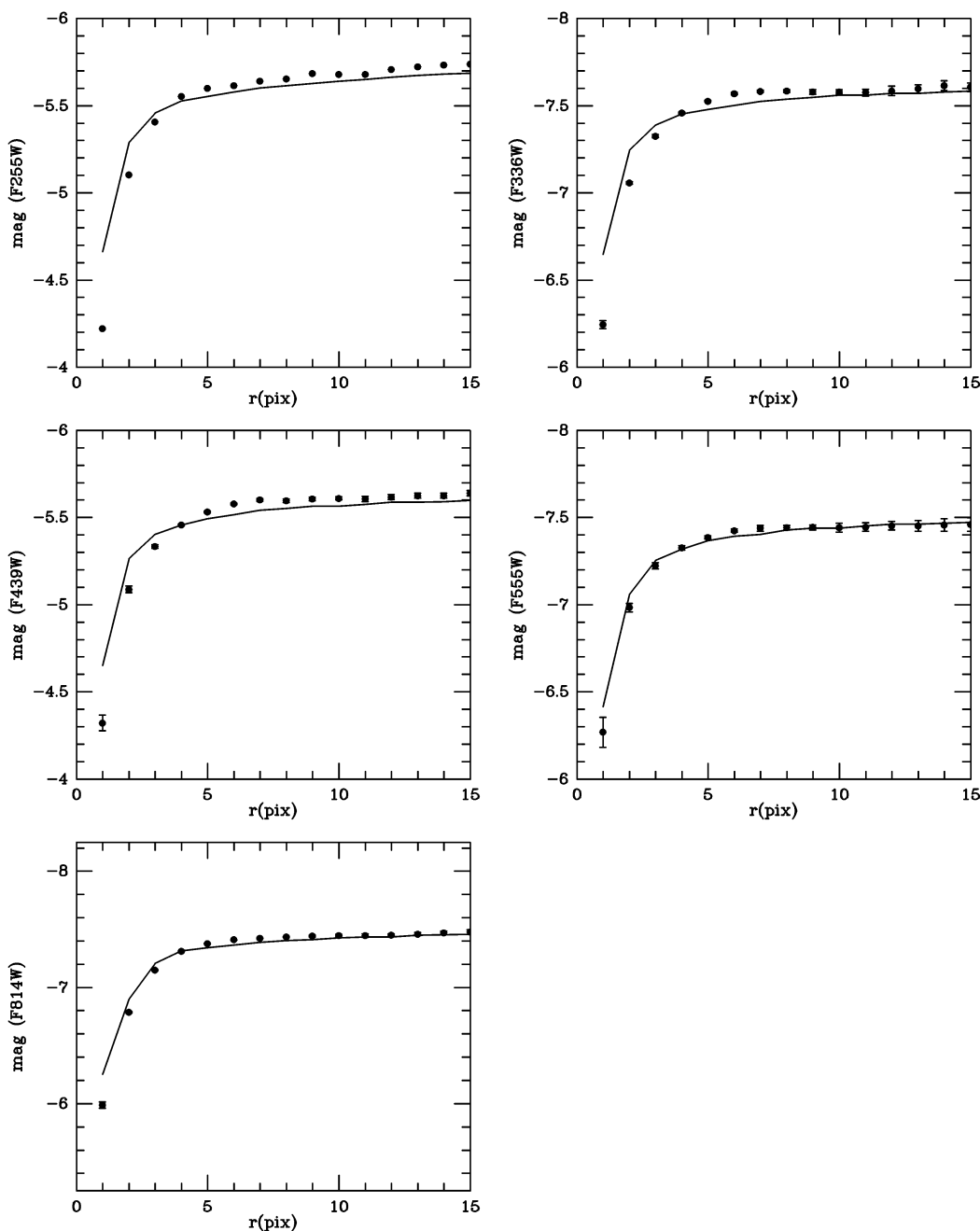


FIG. 10.—Computed encircled energy or growth curves for each filter based only on bright ring clusters. The solid curves are from Holtzman et al. (1995b) for the same filters.

cial clusters with a threshold setting of 3σ . The output from DAOFIND was then plotted on the image to see how well it recovered the input clusters. Although DAOFIND recovered only 76% of the artificial clusters in the magnitude bin 24.75–25.0, it was still fairly easy to identify the missed clusters visually down to this limit, making it possible to get a nearly complete tally. For $V_c > 25.0$, this became less reliable, so we set our completeness limit at $V_c = 25.0$ (Fig. 13, vertical dotted line). For $V_c \leq 25.0$, the luminosity function follows a power law $N(L) \propto L^a dL$ with a slope $a = -2.18 \pm 0.06$. This slope is comparable to slopes found for the luminosity functions of H II regions in Sa–Sc galaxies (Kennicutt, Edgar, & Hodge 1989; Caldwell et al. 1991; Crocker et al. 1996), and also to that derived for blue inner clusters in NGC 7252 (Miller et al. 1997) and other cluster

systems summarized in that paper. As noted by Miller et al., the power-law behavior of the luminosity function of the clusters in ESO 565-11 to a limit of $M_V = -8.9$ could imply a power-law mass function.

5.4. Properties of the Background Starlight

In this section we examine the properties of the starlight that underlies the nuclear ring clusters. As shown in Figure 9, it was possible to separate the ring clusters from the background fairly reliably, something that was not really possible with ground-based images. We are particularly interested in how the orientation of the background starlight changes with wavelength. For this purpose, we computed Fourier amplitudes and phases of the light

TABLE 1
CLUSTER PHOTOMETRY

ID No. (1)	Δx (2)	Δy (3)	V_c (4)	$(U-B)_c$ (5)	$(B-V)_c$ (6)	$(V-I)_c$ (7)	$\sigma(V)$ (8)	$\sigma(U-B)$ (9)	$\sigma(B-V)$ (10)	$\sigma(V-I)$ (11)
28	6.91	4.17	22.54	-0.43	0.06	0.67	0.04	0.08	0.09	0.07
98	-2.02	-4.19	22.64	-0.57	0.01	0.60	0.04	0.08	0.09	0.07
125	-8.29	-0.52	21.92	-0.69	-0.13	0.52	0.03	0.05	0.07	0.05
130	-9.04	0.05	21.67	-0.71	-0.01	0.51	0.03	0.05	0.06	0.05
200	6.81	0.00	22.19	-0.64	0.13	0.45	0.03	0.06	0.07	0.06
247	4.05	-3.62	22.24	-0.77	-0.12	0.22	0.03	0.06	0.07	0.07
266	-3.50	4.45	22.80	-0.83	-0.21	-0.05	0.05	0.07	0.10	0.10
287	-1.63	-4.33	22.40	-0.72	0.06	0.40	0.04	0.07	0.08	0.07
290	-2.18	-4.77	21.83	-0.81	-0.02	0.20	0.03	0.05	0.06	0.05
292	-6.75	1.36	21.97	-0.67	0.00	0.63	0.03	0.05	0.07	0.05
318	-4.01	-4.57	21.30	-0.32	0.56	0.71	0.02	0.05	0.05	0.04
320	-8.78	2.08	22.22	-0.77	-0.25	0.06	0.03	0.05	0.07	0.07
324	-6.96	-0.91	22.62	0.05	0.11	0.65	0.04	0.12	0.09	0.07
361	-10.03	-1.32	22.60	-0.19	0.17	0.42	0.04	0.10	0.09	0.07
380	7.75	2.29	20.22	-0.87	-0.18	-0.01	0.02	0.03	0.04	0.03
386	8.36	-1.88	22.68	-0.63	-0.02	0.45	0.10	0.09	0.15	0.13
387	8.25	-1.80	22.63	-0.66	-0.05	0.66	0.06	0.07	0.10	0.09
388	3.93	3.85	22.88	-0.62	0.09	0.64	0.15	0.13	0.23	0.19
404	-4.02	4.53	20.74	-0.86	-0.16	0.02	0.02	0.04	0.04	0.04
412	-0.83	-4.66	20.74	-0.84	0.09	0.07	0.02	0.04	0.04	0.04
413	-7.85	4.47	22.58	-0.89	-0.14	0.26	0.04	0.06	0.09	0.08
422	-8.38	0.04	22.94	-0.71	-0.27	0.60	0.05	0.07	0.11	0.08
488	2.41	4.16	22.90	-0.36	0.35	0.58	0.08	0.12	0.15	0.12
519	-3.82	3.51	22.82	-0.73	-0.02	0.38	0.05	0.08	0.10	0.09
525	-0.08	-4.55	21.16	-0.67	0.16	0.29	0.02	0.04	0.05	0.04
529	-1.01	-4.59	21.09	-0.77	0.00	0.26	0.02	0.04	0.05	0.04
531	-7.78	4.30	22.00	-0.90	-0.11	0.11	0.03	0.05	0.07	0.06
544	-7.38	1.87	22.61	-0.56	0.11	0.35	0.09	0.11	0.16	0.13
545	-7.40	1.71	20.81	-0.75	-0.12	0.38	0.02	0.04	0.05	0.03
553	-8.85	3.28	22.91	-0.75	-0.41	0.05	0.05	0.07	0.10	0.11
570	-8.29	0.29	22.78	-0.60	-0.13	0.57	0.05	0.08	0.10	0.08
589	-8.84	-2.10	22.86	-0.24	0.20	0.96	0.05	0.12	0.11	0.07
601	4.21	3.97	20.77	-0.61	0.21	0.57	0.02	0.04	0.04	0.03
616	7.16	-1.98	21.59	-0.81	-0.18	0.09	0.03	0.04	0.06	0.05
659	-4.15	4.22	21.92	-0.88	-0.09	0.35	0.03	0.05	0.06	0.05
701	-0.09	4.83	22.84	-0.50	0.69	1.12	0.07	0.17	0.18	0.12
739	-8.49	-2.12	22.90	-0.67	0.05	0.13	0.09	0.13	0.18	0.16
768	4.12	4.00	22.83	-0.80	0.19	0.24	0.16	0.15	0.23	0.27
769	7.65	2.35	22.55	-0.77	0.29	0.46	0.15	0.15	0.22	0.20

NOTE.—Table 1 is presented in its entirety in the electronic edition of the *Astronomical Journal*. A portion is shown here for guidance regarding its form and content.

distribution within circular annuli spaced by $0''.2$ in radius from the center. The right panels of Figure 14 show the relative amplitudes and phases (position angle measured east from north) of the 2θ component of the background luminosity distribution with different line types for U , B , V , and I . For comparison, the left panels of Figure 14 show the same quantities for the ring only. For both the ring and the background, the relative amplitude of the 2θ component decreases smoothly from U to I . However, while the phase changes little in the ring cluster system from U to I , the phase of the background starlight changes significantly. Table 3 summarizes these changes. In the radius range $7''.5 \leq r \leq 9''.0$, the phase of the ring changes from 89° to 94° , while that of the background starlight changes from 100° to 129° . The direction perpendicular to the bar corresponds to a position angle of 118° . If the U -band ring represents the youngest population in this comparison and the I -band background represents the oldest, then the phase changes by 40° in the sense that the background starlight is nearly aligned perpendicular to the bar while the young ring has

an intermediate angle to the bar. Figure 15 shows an ellipse fit to an I -band isophote having a radius of $8''.9$. After rejecting points affected by the dust lanes, this isophote is aligned exactly perpendicular to the bar in projection.

Another way of examining the properties of the background starlight is shown in Figure 16. For this plot, the fluxes on the cluster-corrected images (as in Fig. 9, *bottom left*) were integrated in 72 apertures $1''$ in diameter along a circle having a radius of $8''$ from the center. The phase changes shown in the right panel of Figure 14 should be accompanied by color changes along the circle. Figure 16 shows the colors as a function of position angle relative to the position angle of the major axis of the $H\alpha$ nuclear ring from BPC, folded around the two halves of the main circle to improve the signal-to-noise ratio and after removal of any points affected by the dust lanes. This plot shows that $V-I$, $B-V$, and $B-I$ follow an asymmetric pattern relative to the $H\alpha$ ring, which we suggest is due to a change in the mean age of the stellar population with position angle $\phi - \phi_{\text{ring}}$. From $B-V$ and a $Z = 0.02$ BC96 model, the age

TABLE 2
ULTRAVIOLET PHOTOMETRY OF 21 STELLAR OBJECTS

Id. No.	$(m_{F255W})_c$	$\sigma(m_{255W})$	$(m_{F255W}-V)_c$	$\sigma(m_{F255W}-V)$
125.....	20.07	0.18	-1.85	0.18
130.....	20.15	0.16	-1.53	0.16
247.....	20.38	0.20	-1.87	0.20
266.....	20.95	0.32	-1.86	0.33
287.....	20.69	0.22	-1.72	0.23
290.....	20.13	0.15	-1.70	0.15
292.....	20.90	0.33	-1.06	0.33
320.....	19.93	0.14	-2.29	0.15
380.....	18.19	0.06	-2.02	0.06
404.....	18.81	0.10	-1.94	0.10
412.....	18.91	0.08	-1.83	0.08
413.....	20.35	0.18	-2.23	0.19
519.....	20.89	0.29	-1.92	0.29
525.....	20.59	0.23	-0.57	0.23
529.....	19.68	0.16	-1.41	0.16
531.....	20.38	0.21	-1.62	0.21
545.....	19.09	0.08	-1.72	0.09
601.....	19.79	0.13	-0.98	0.13
616.....	19.66	0.12	-1.93	0.13
659.....	19.99	0.15	-1.93	0.16
739.....	20.57	0.22	-2.33	0.24

change would be from 10^9 yr at $\phi - \phi_{\text{ring}} \approx 0^\circ$ to 2×10^{10} yr for $\phi - \phi_{\text{ring}} \approx 115^\circ$, the position angle of the bar. The cause of this phase change could be gravity torques operating on aging ring stars. Note that if stars born in the ring simply circled around the ring as they aged, we would see an old ring underlying the young one and the profiles in Figure 16 would not be asymmetric.

5.5. The Nuclear Region

The bulge in ESO 565-11 is well defined, and the region where it dominates is well inside the nuclear ring. Figure 17 shows I -band luminosity profiles of the bulge along axes parallel and perpendicular to the ring major axis. The bulge is nearly round, so these profiles are very similar. Both show a steeply declining behavior inside and outside of a prominent inflection point, which gives the bulge a somewhat sharp edge. Faber et al. (1997) discuss the central profiles in a large sample of E galaxies and some bulges. The bulge of ESO 565-11 does not appear to be of the core type, but could be of the power-law type.

Ellipse fits to the bulge region are shown for V and I in Figure 18. These were made using the IRAF-based GALPHOT package of ellipse-fitting routines. In these passbands a minimum in axis ratio occurs near a radius of

TABLE 3
MEAN RELATIVE $m = 2$ FOURIER AMPLITUDES AND PHASES^a

FILTER	RING		BACKGROUND	
	$\langle I_2/I_0 \rangle$	$\langle \theta_2 \rangle$ (deg)	$\langle I_2/I_0 \rangle$	$\langle \theta_2 \rangle$ (deg)
F336W.....	1.35 ± 0.07	88.6 ± 3.5	0.69 ± 0.02	99.9 ± 0.8
F439W.....	0.56 ± 0.06	91.4 ± 2.8	0.40 ± 0.03	115.9 ± 0.4
F555W.....	0.34 ± 0.04	92.0 ± 3.0	0.24 ± 0.02	123.1 ± 0.5
F814W.....	0.23 ± 0.02	93.8 ± 2.5	0.15 ± 0.01	128.9 ± 1.2

^a Over radius range $7''.5$ to $9''.0$; errors listed are those of the mean.

$0''.15$. Although the depth of the minimum is very different for V compared with I , the position angle is very similar in both filters across the dip. The minimum could indicate the presence of a small bar or oval inside the bulge. However, nuclear dust may be impacting the appearance of this feature. To examine this, we show in Figure 19 two images: the left panel shows residuals in the V -band image of the bulge from a model of it constructed from the ellipse fits in Figure 18. This shows the X pattern and a spiral-shaped minimum in residual intensity. The right panel of Figure 19 shows a $V-I$ color index map coded such that redder areas are lighter and bluer areas are darker. This shows a very similar pattern of red colors as the residual ellipse fit map and suggests that the structure in this area is mainly caused by dust. In the I band the “microbar” is really a micro-oval. It is unclear whether imaging at longer wavelengths would make this feature totally disappear.

6. ANALYSIS OF THE NEAR-INFRARED LIGHT DISTRIBUTION

In this section, we attempt to determine the gravitational potential of ESO 565-11 by using the H -band light distribution under the assumption of a constant mass-to-light ratio. The procedure involves the following steps: (1) subtraction of an H -band bulge model; (2) removal of the light of young star clusters from the H -band image; (3) deprojection of the residual old disk light; (4) transformation of this light distribution to a disk gravitational potential; and (5) assessment of other components to the mass distribution.

6.1. Bulge Model

The resolution of the H -band image is so low that it is not possible to derive a reliable bulge model from that image alone. Instead, we believe it is reasonable to bootstrap an H -band bulge model from one derived in the I band. BPC used a combination of ellipse fit and elliptically averaged profiles in B and I to derive a standard $r^{1/4}$ bulge and exponential disk model of ESO 565-11. The structure of ESO 565-11 is so complex and the galaxy is so face-on that use of major- and minor-axis profiles for this purpose, as is often done (e.g., Kormendy 1977; Kent 1986), is impractical. BPC derived a disk effective radius of $27''$ and a bulge effective radius of $9''.5 \pm 3''.0$. Figure 20 shows the HST I -band surface brightness in ESO 565-11 along position angle 93° versus $r^{1/4}$, with the BPC bulge and disk models indicated. The BPC bulge model is a reasonable representation of the data. Larger effective radii for the bulge would predict excessive bulge light at large radii. To apply this model in the H band, we require that the bulge at H contribute at least as much to the total luminosity as it does at I . This is 26%, which requires that the $I-H$ color of the bulge be 1.99 if the total H -band magnitude is 9.85. This is similar to the total galaxy color of $(I-H)_T = 1.98$. Probably the bulge is more important at H than at I , but the difference is not important for our models. We ignore any possible $I-H$ color gradient in the bulge, since we cannot assess it reliably.

After deciding on the bulge effective radius, surface brightness, and color, an image of the bulge was created at the resolution of the HST I -band image, and then this model was degraded to the resolution of the H -band image by binning the array into a 25×25 pixel block average and then matching the FWHM of stellar profiles on the H -band

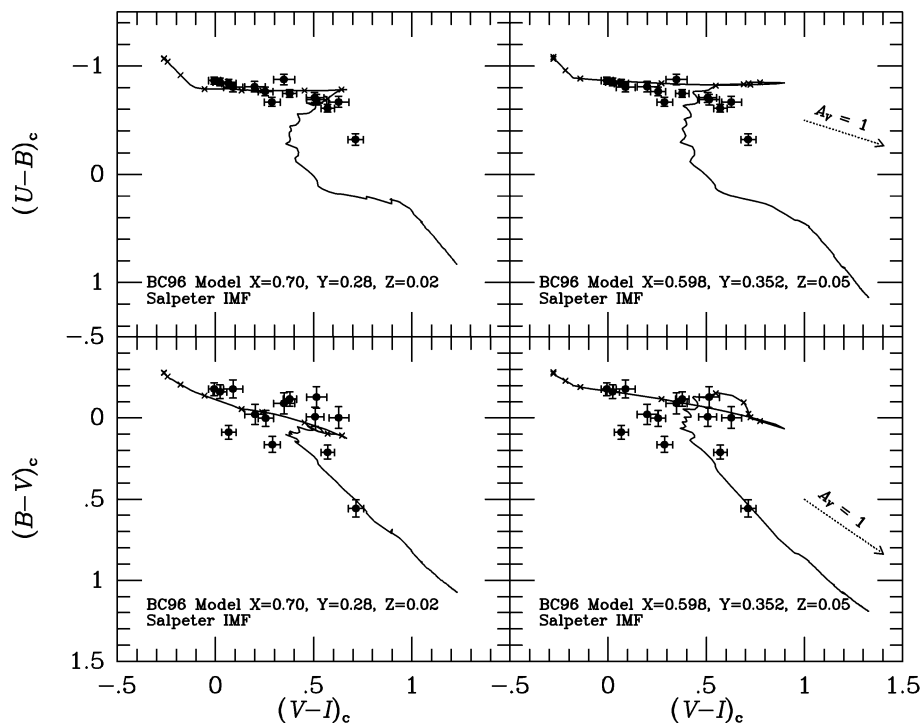


FIG. 11a

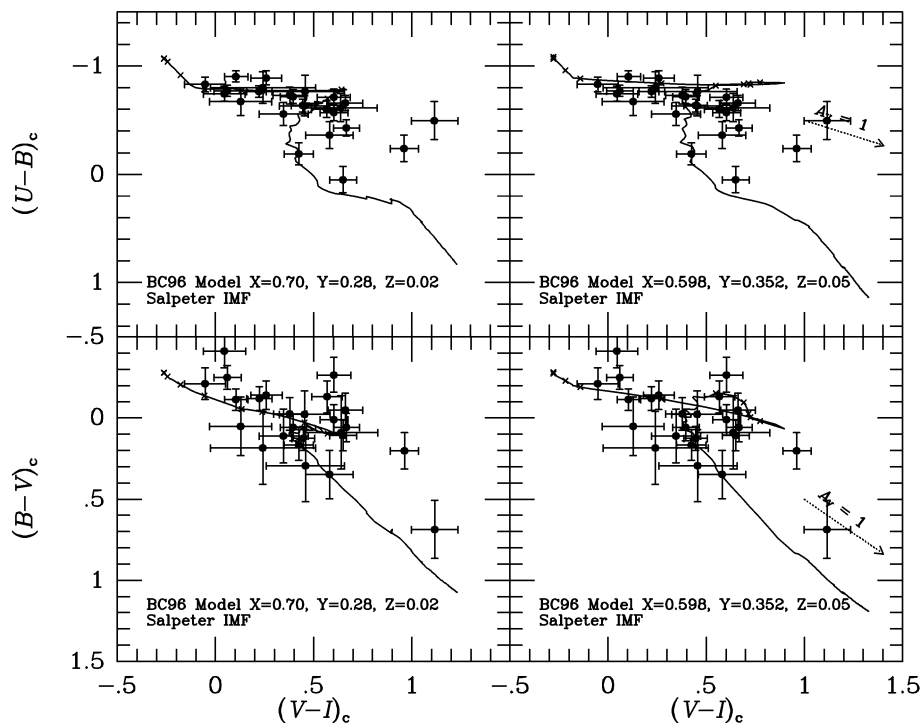


FIG. 11b

FIG. 11.—Two-color plots for ring clusters in different magnitude ranges: (a) $V_c \leq 22.0$; (b) $22.0 < V_c \leq 23.0$; (c) $V_c \leq 24.0$. No clusters were found to be brighter than $V_c = 20.0$. The solid curves on each plot represent instantaneous-burst isochrone synthesis models from BC96. Two different models are illustrated, and the abundance parameters and IMF are specified in the legends. Also shown are reddening vectors for a visual extinction of $A_V = 1.0$ mag. The subscript c on the colors only means that the colors are corrected for Galactic extinction, not internal extinction. Crosses on the model curves are separated by 1 Myr and are indicated only over the range of 1–10 Myr.

image using Gaussian smoothing. The resulting inferred H -band bulge model was then subtracted from the H -band image.

In order to assess the influence of the bulge model on our simulations, we also computed a second, completely differ-

ent model. One way of interpreting the central region is that the light distribution is the sum of a spherical bulge and a nuclear lens of relatively uniform surface brightness in I . In the radius range $4''.5$ to $5''$, the lens has a surface brightness of $\mu_I = 19.09$ mag arcsec $^{-2}$. After subtraction of this level

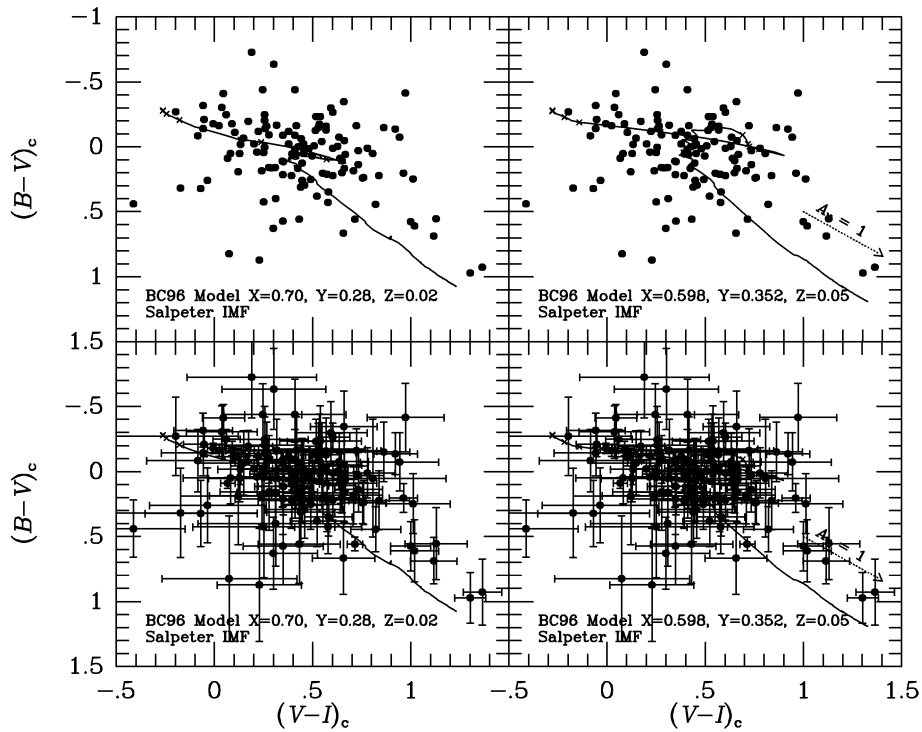


FIG. 11c

from the profile along position angle 93° (Fig. 17), the residual profile can be well represented by the sum of two exponentials with scale lengths of $0''.14$ and $0''.89$. Thus, the bulge is confined only to the central few arcseconds in this representation. The main difference with the $r^{1/4}$ model is

that the double exponential model contributes only 5.5% of the total I -band luminosity. As for the $r^{1/4}$ model, an image of this model was made, scaled to the H band, and then subtracted from the H -band image. Our two bulge models hopefully bracket the true bulge properties in ESO 565-11.

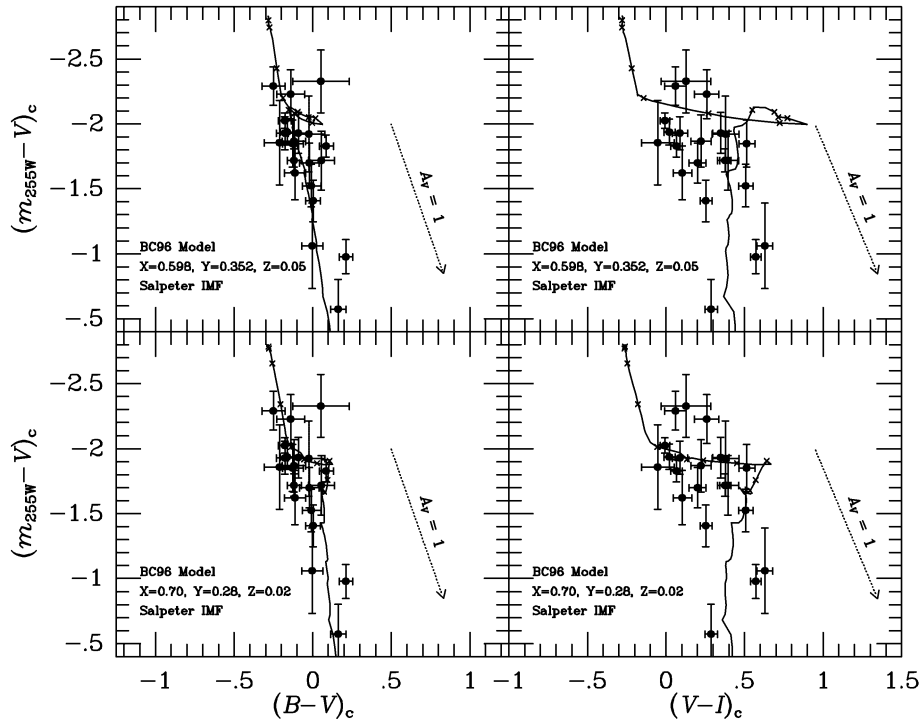


FIG. 12.—Two-color plots for 21 ring clusters detected in the F255W filter. The solid curves are based on interpolations between $2200 - V$ and $2700 - V$ instantaneous-burst model colors from BC96. Reddening vectors for $A_V = 1.0$ mag are shown. Crosses on the model curves are separated by 1 Myr and are indicated only over the range of 1–10 Myr.

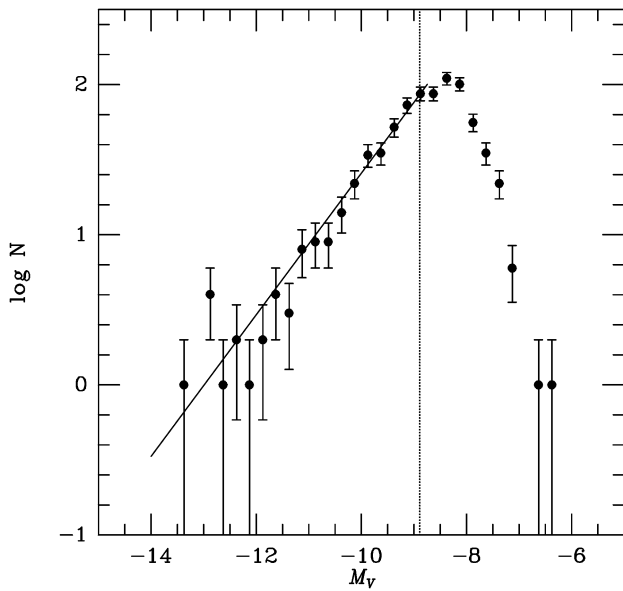


FIG. 13.— V -band luminosity function of the ring clusters, assuming a distance of 60 Mpc and after correction only for Galactic extinction. The vertical dotted line represents the estimated completeness level of the cluster identifications. The solid line represents a power-law fit to the bright, complete end of the luminosity function.

6.2. Correcting for the Young Clusters in the Ring

The derivation of the gravitational potential of ESO 565-11 from the bulge-corrected image explicitly assumes that the H -band light distribution traces the mass distribution of old stars and is characterized by a constant mass-to-light ratio. However, as we noted in § 3.3, in the area of the nuclear ring the light distribution is knotty most likely because young red supergiants in the super-star clusters in the ring are prominent at H . Thus, the H -band light distribution in this region is not tracing only the old stellar mass. Using the I -band HST net cluster image (i.e., corrected for full background), we have attempted to remove the light of some of the young clusters by inferring an expected $I-H$ color of 1.44 from the BC96 synthesis models and applying a mean reddening correction corresponding to $E(B-V) = 0.1$ mag for the brighter and least reddened clusters. These numbers were used to compute a scale factor for conversion to H -band intensities and then the image of the ring was degraded to the resolution of the H -band image. The scale factor derived removed the clusters well and did not appear to over- or undercorrect for them. Still, the procedure cannot be expected to fully correct for the clusters, especially the most reddened ones.

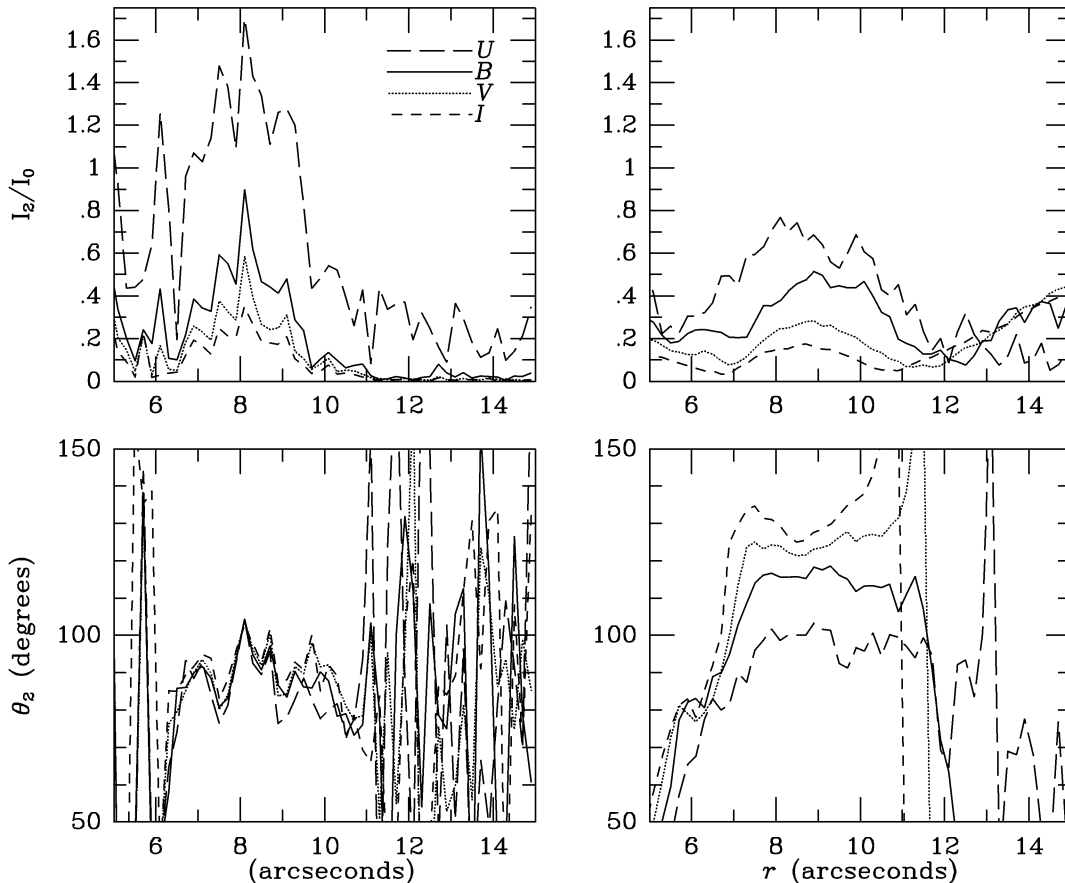


FIG. 14.—Relative amplitudes I_2/I_0 and phases θ_2 of the $m = 2$ Fourier component of the light distributions in $UBVI$, based on circular averages; θ_2 corresponds to a normal position angle measured eastward from north. The left panels are based on the pure cluster images (as in Fig. 9, bottom right), while the right panels are based on the cluster-free images (as in Fig. 9, bottom left). Note the significant phase shift in the background starlight with increasing filter effective wavelength.

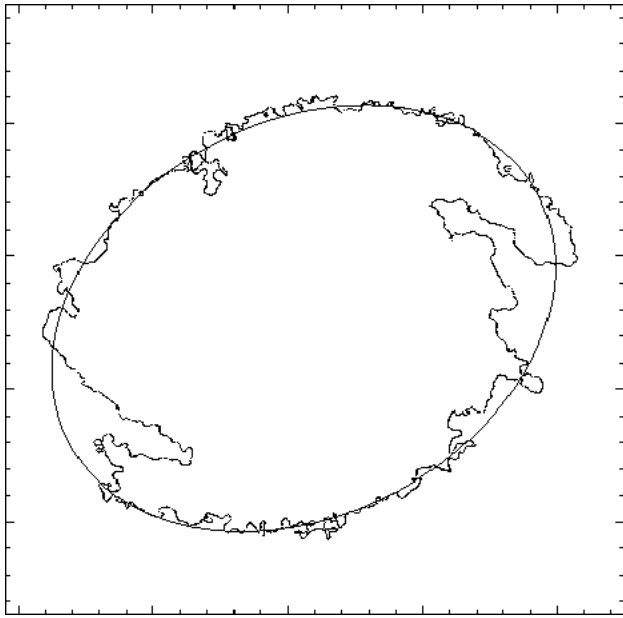


FIG. 15.—Ellipse fit to an I -band isophote whose radius is $9''$. The fit ignored the obvious effect of the dust lanes. This isophote is oriented perpendicular to the primary bar of ESO 565-11. Each tick mark is separated by $0''.91$. North is at the top and east is to the left.

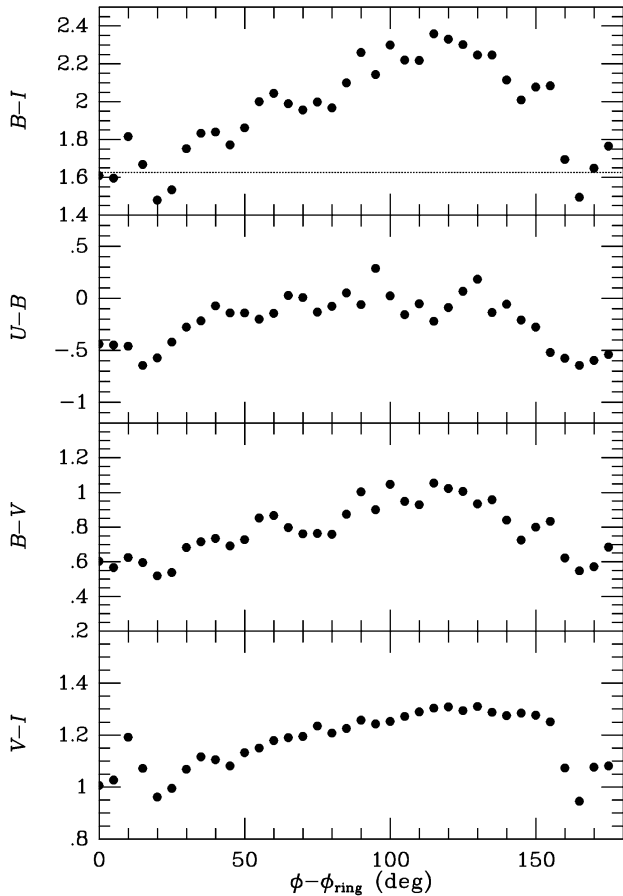


FIG. 16.—Average colors along a circle located at a radius of $8''$ vs. angle relative to the major-axis position angle of the $H\alpha$ nuclear ring studied by BPC. Two halves of the circle have been averaged to improve signal-to-noise ratio. The plot shows an asymmetric color profile that reflects a gradual population change with increasing angle from the ring. Points connected with the dust lanes in the ring are excluded from the plot.

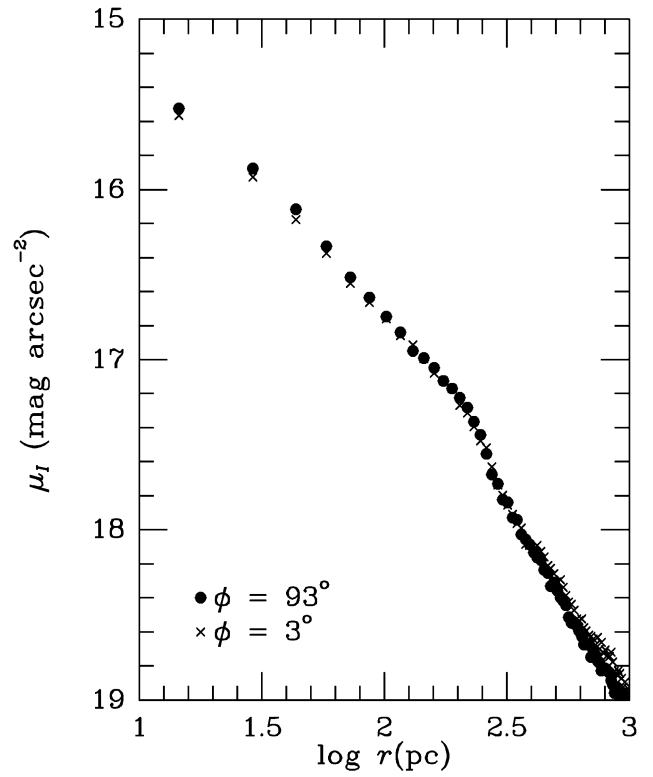


FIG. 17.— I -band luminosity profiles of the bulge of ESO 565-11 along the nuclear ring major axis (circles) and the nuclear ring minor axis (crosses).

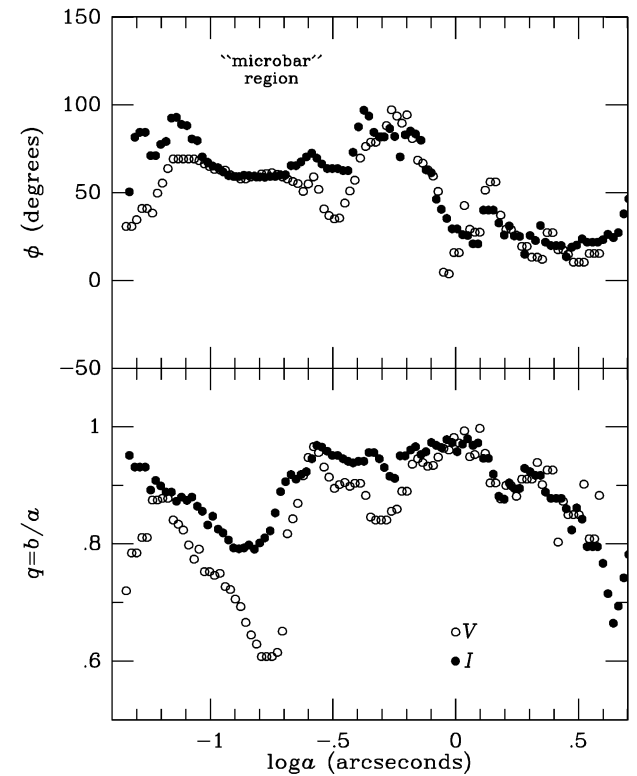


FIG. 18.—Results of ellipse fits to isophotes in the bulge region. The parameter q is the apparent axis ratio, while the parameter ϕ is the apparent major-axis position angle. The radius range labeled “microbar region” includes the small central oval inside of the apparent X-shaped feature.

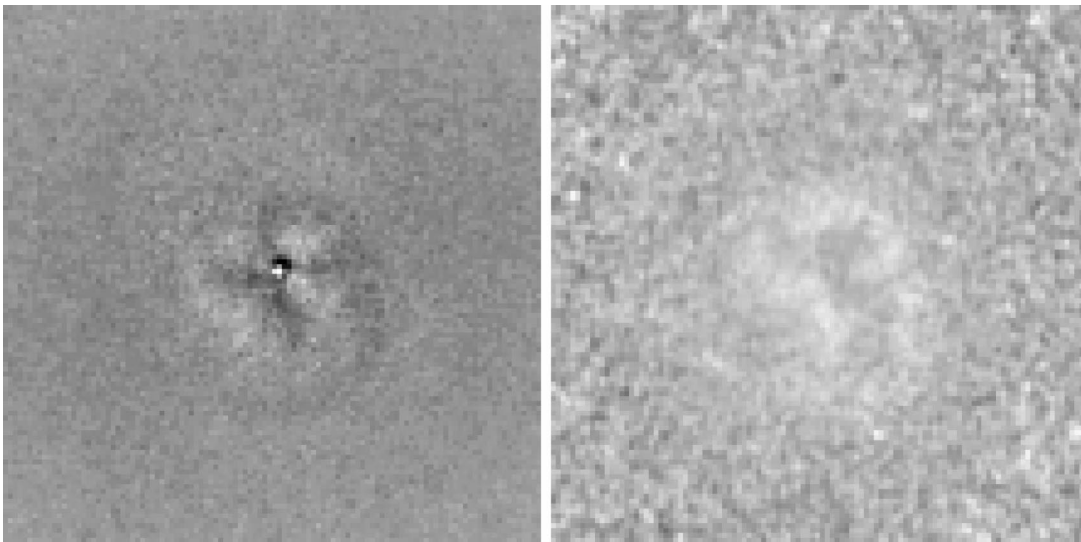


FIG. 19.—*Left*: residuals from an ellipse-fit model to the V -band bulge isophotes, revealing the X pattern in the center. *Right*: $V-I$ color index map of the same region, coded such that redder features are lighter. This suggests that some of the structure seen in the X is due to extinction. Each frame is $5'' \times 5''$ in area. North is at the top and east is to the left.

6.3. Deprojection of the Old Disk Light

The next step was to deproject the net disk image (corrected for both the bulge light and the young clusters). This requires knowledge of the inclination and line of nodes, estimates of which were made by BPC. Based on fits of ellipses to faint outer disk isophotes, and assuming axisymmetry at these radii, BPC derived an inclination of 33° and a major-axis position angle of 72.5° . However, the kinematics of H II regions in the disk, based on Fabry-Perot interferometry, suggested that a lower inclination may be

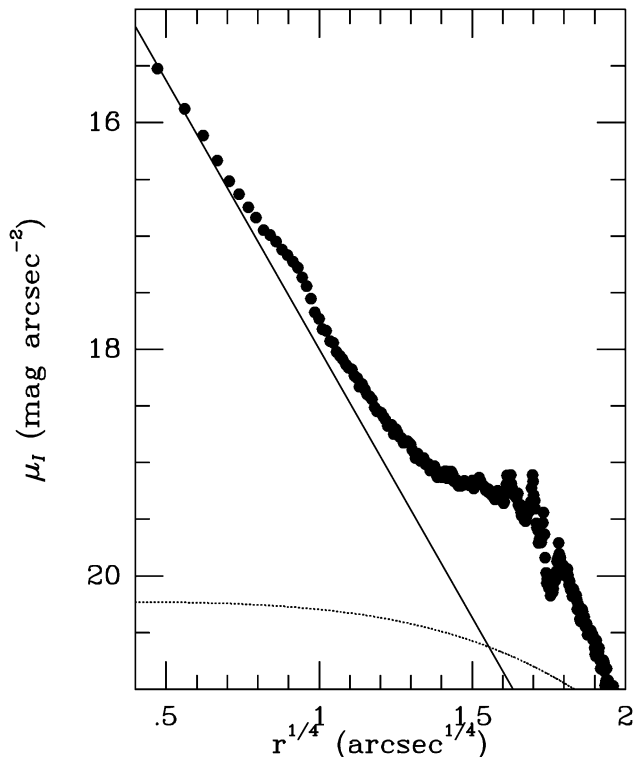


FIG. 20.—An $r^{1/4}$ bulge model (solid line) of ESO 565-11 superposed on the *HST* I -band luminosity profile in position angle 93° . A disk model (dotted curve) is also shown. These photometric models are from BPC.

more correct. Analysis of the velocity field indicated a kinematic line of nodes in very good agreement with the photometric major-axis position angle, but the implied rotation velocities for an inclination of 33° were uncharacteristically low for the type of the galaxy. The rotation curve derived by BPC also showed two levels of rotation, a low level in the region of the nuclear ring, and a higher level in the region of the inner pseudoring. As shown in the next section, the inferred gravitational potential provides little support for the change, which we suggest now could be an artifact of incomplete velocity coverage and noncircular motions in the inner ring region. Because of this, we have used the velocities in the nuclear region alone, where the velocity coverage is complete, to compute an inclination from the I -band Tully-Fisher relation derived by Tully et al. (1998) and assuming a distance of 60 Mpc. From the T-F relation and the inferred absolute magnitude of the galaxy, we inferred an expected maximum rotation velocity of about 190 km s^{-1} and an inclination of 11° . A program called GAL (van Moorsel & Wells 1985), from the Astronomical Imaging Software Package (AIPS), was used to compute a revised kinematic line-of-nodes position angle, ϕ_n ; this yielded a value of 71° . With these orientation parameters, the net H -band image was deprojected using IRAF routine IMLINTRAN in flux-conserving mode. The much lower inclination from this analysis compared with the photometric value is noteworthy. The true inclination may be between 11° and 33° . A rotation curve was recomputed for the galaxy's inner regions using $\phi_n = 71^\circ$ and $i = 11^\circ$ and is used in our subsequent analysis. This is a major source of uncertainty in our mass-to-light ratio estimates.

6.4. Computation of the Gravitational Potential

The gravitational potential of the disk of ESO 565-11 was computed using a program described by Quillen, Frogel, & González (1994). The method uses a fast Fourier transform on a rectangular coordinate grid and allows for finite thickness of the disk. The vertical scale height h of the disk was computed as $(1/12)h_D$, where h_D is the radial exponential scale length in the IR. We used the value computed for the I

band in BPC to estimate a scale height of $h = 1''.3 = 390$ pc, because it is more accurate than what we can derive from our H -band image. We used a convolution function appropriate for a vertical disk density proportional to $\text{sech}^2(z/h)$ (see eq. [3.4] of Quillen et al.). For the case of the $r^{1/4}$ bulge model, the resulting deprojected image, the total disk potential, and the axisymmetric and nonaxisymmetric parts of the potential are shown in Figure 21. The nonaxisymmetric part shows the primary bar mainly as two “ansae” and the misaligned oval as a pair of spiral arms.

Figure 22 shows the relative amplitude of the $m = 2, 4$, and 6 components of the disk potential in Figure 21, and the phase of the $m = 2$ component, as a function of radius. The amplitude of the $m = 2$ component reaches 9% of the disk axisymmetric background. The misaligned oval produces a secondary bump in the relative $m = 2$ amplitude that reaches 7% of the axisymmetric background. The two components are nearly equally important, but they differ in

phase by about 50° . Higher inclinations than 11° make the outer component comparable to or even more important than the bar. These amplitudes decrease slightly for the double exponential bulge model, since there is more axisymmetric disk light in this case.

6.5. Numerical Simulations

We have used the derived potential to make “sticky particle” simulations of ESO 565-11 (see Schwarz 1981; Shaw et al. 1993; Byrd et al. 1994; Sempere et al. 1995; Rautiainen et al. 1996). The idea is to follow the evolution of a cloud particle disk in this potential to derive the likely pattern speed of the bar. The clouds are allowed to collide and lose some fraction of their kinetic energy as a result. The codes we have used are described by Combes & Gerin (1985) and the procedure is described in Sempere et al. (1995). A total of 19,000 particles are used to represent the cloud disk.

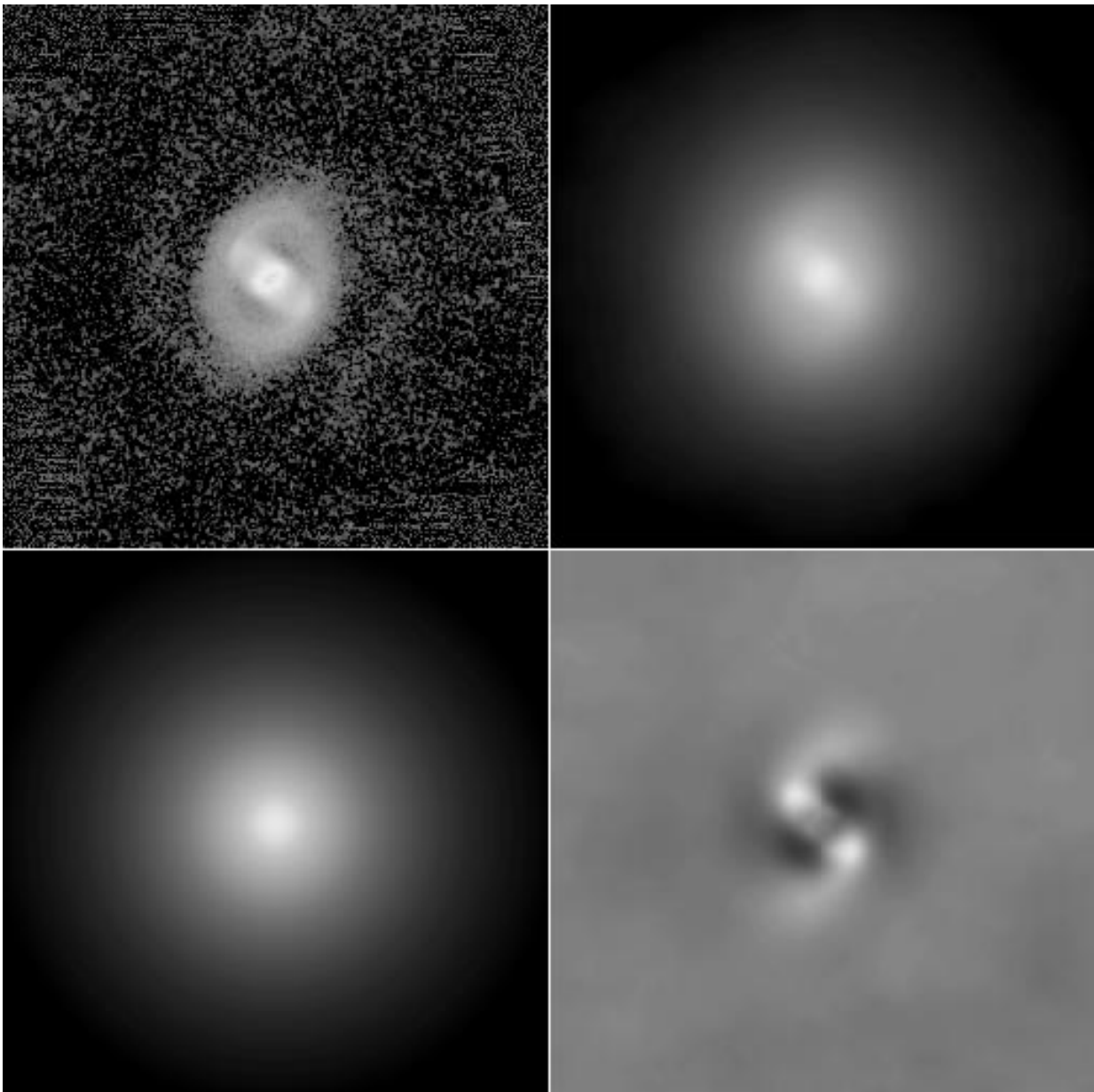


FIG. 21.—Images of the disk gravitational potential in ESO 565-11, after subtraction of the $r^{1/4}$ bulge model in Fig. 20. *Top left*, deprojected H -band image; *top right*, derived gravitational potential; *bottom left*, axisymmetric ($m = 0$) part of the potential; *bottom right*, nonaxisymmetric ($m > 0$) part of the potential.

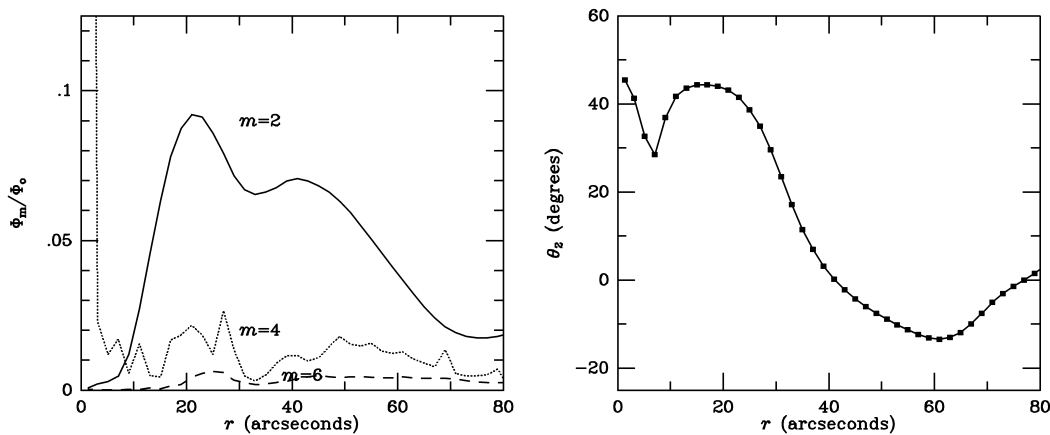


FIG. 22.—*Left*, relative amplitudes of the $m = 2, 4$, and 6 components of the disk gravitational potential in Fig. 21 vs. radius; *right*, phase of the $m = 2$ component of the potential vs. radius.

The first step in the analysis is to derive the axisymmetric rotation curve of the disk from the gravitational potential and to deduce the parameters that might characterize the bulge and outer halo. The bulge light profile was converted to a rotation curve assuming a spherical shape and a constant mass-to-light ratio with radius, using a program written by A. Kalnajs & S. Hughes. For input into the collision code, it was necessary to represent this rotation curve with Plummer models (Binney & Tremaine 1987).

Lacking any reliable constraints on the rotation curve in the outer parts, we used another Plummer model to force the outer rotation curve to be relatively flat at a level close to 190 km s^{-1} . Reasonable models for the two bulge representations are shown in Figure 23, but the halo choice impacts any assertion we make about resonance locations in the outer disk.

The Plummer models are defined by an asymptotic mass M_p and a characteristic radius b . For the $r^{1/4}$ bulge, the two

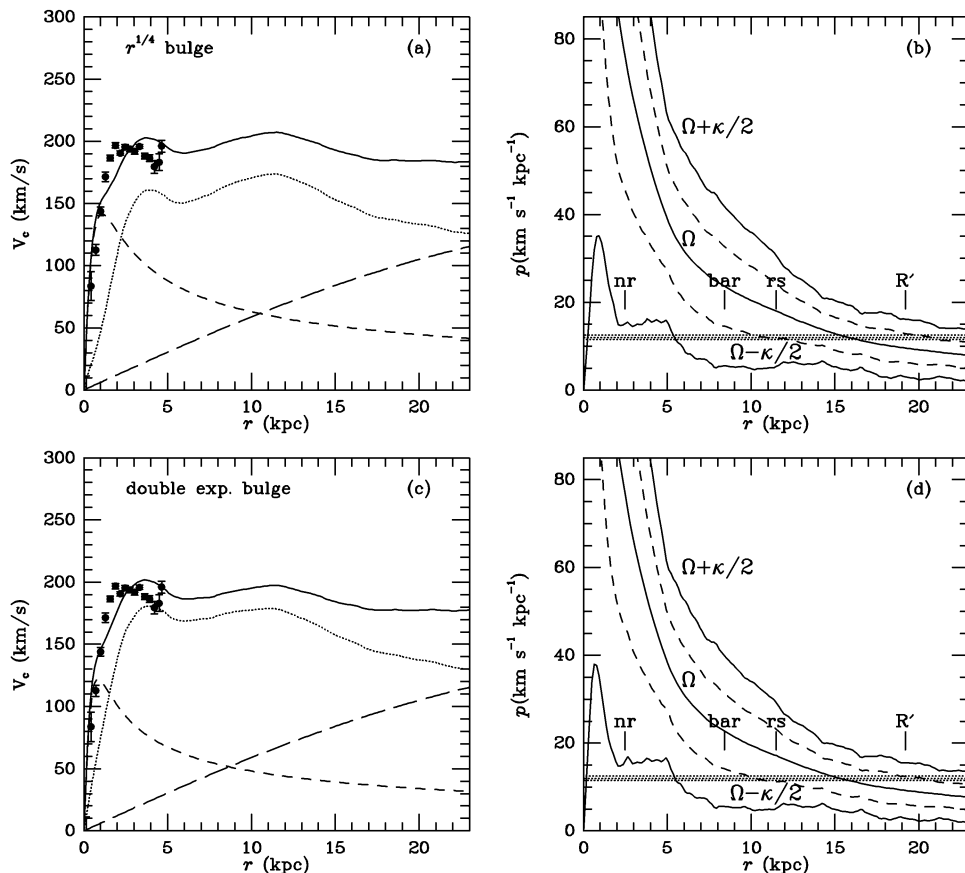


FIG. 23.—(a) Adopted mass model of ESO 565-11 for the $r^{1/4}$ bulge model: *dotted curve*, disk; *short-dashed curve*, bulge; *long-dashed curve*, halo; *solid curve*, total model. (b) Lindblad precession frequencies $p(\Omega, \kappa)$ for the $r^{1/4}$ bulge model, where Ω is the circular angular velocity and κ is the radial epicyclic frequency. The unlabeled dashed curves are for $p = \Omega \pm \kappa/4$. The radii of the nuclear ring (nr), bar, inner pseudoring (rs), and outer pseudoring (R') are indicated. The dotted horizontal band is for a pattern speed of $12 \pm 0.5 \text{ km s}^{-1} \text{ kpc}^{-1}$. (c, d) Same as (a) and (b) for the double exponential bulge model, respectively.

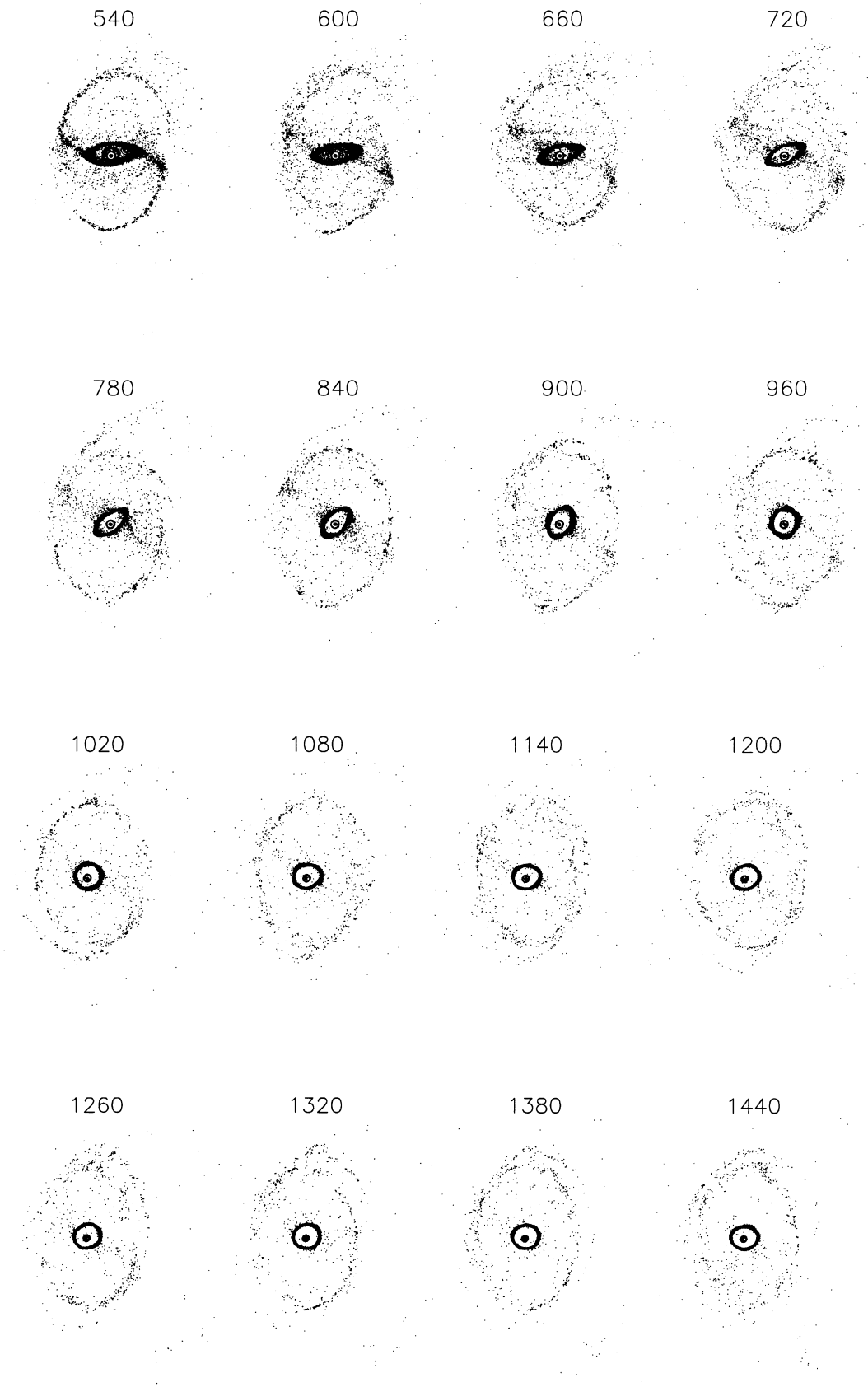


FIG. 24a

FIG. 24.—(a) Particle plots for simulations of ESO 565-11 for a pattern speed of $12 \text{ km s}^{-1} \text{ kpc}^{-1}$, a bar turn-on time of 450 Myr, and the $r^{1/4}$ bulge model. (b) Same as (a), but for the double exponential bulge model. In both sets of simulations, the time in Myr of the frame is indicated above the frame. Time frames earlier than 540 Myr are during the bar turn-on period and are not shown. Time frames later than 1440 Myr are also not shown since little change took place in the simulated gas distributions. For scale, each frame is separated by 30 kpc.

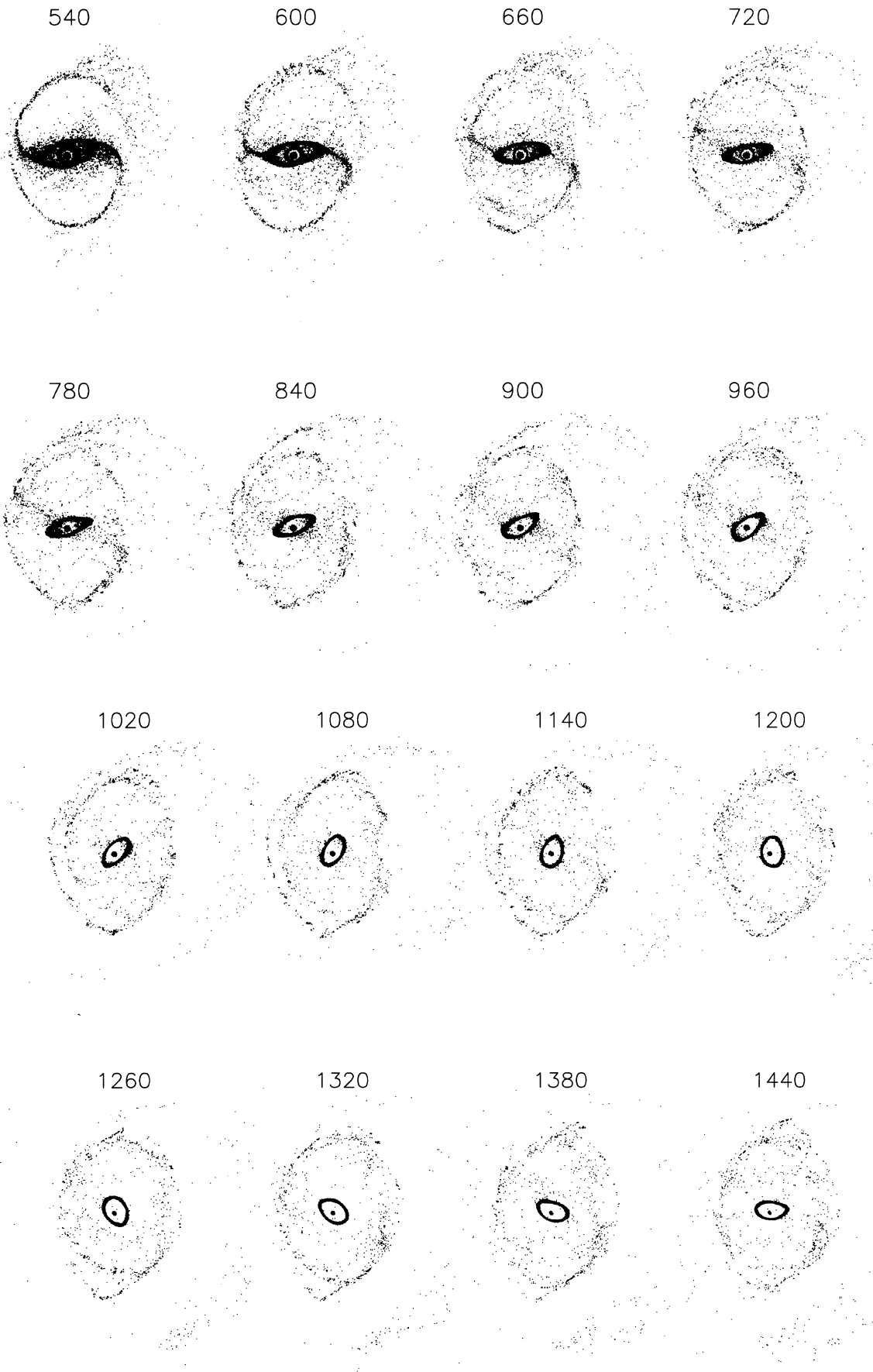


FIG. 24b

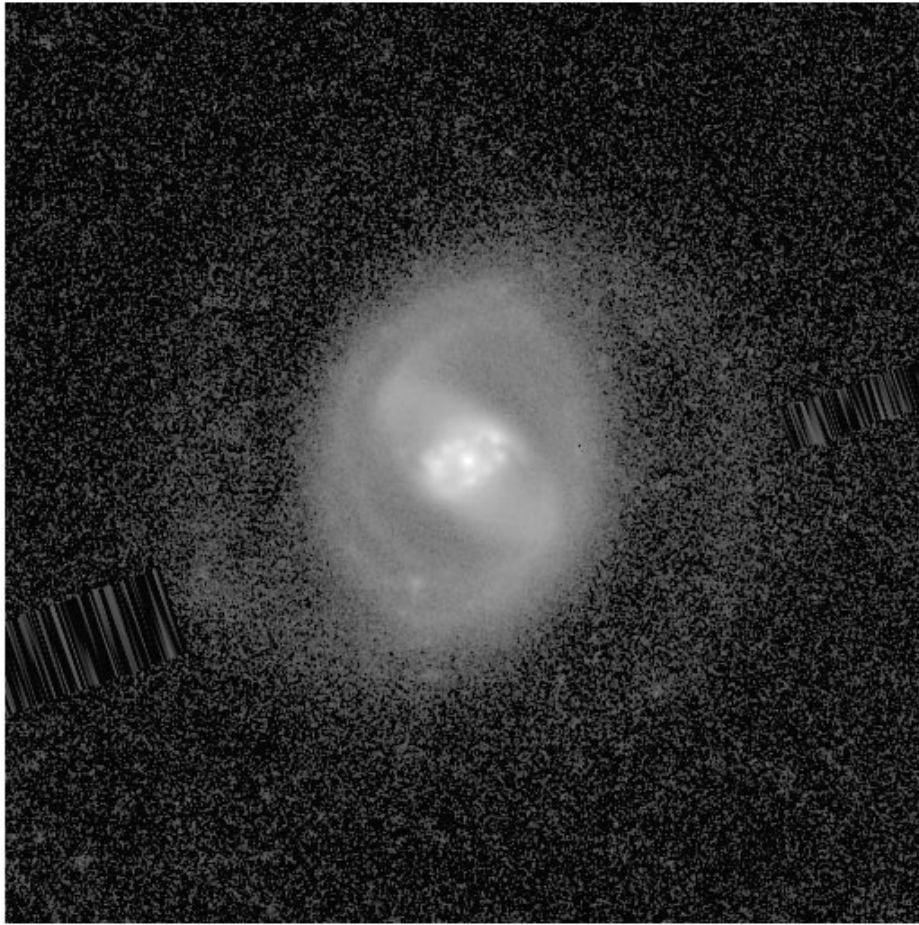


FIG. 25.—Deprojected B -band image of ESO 565-11, based on the Tek CCD image used by BPC. The inclination and line-of-nodes position angle assumed were 11° and 71° , respectively. The field shown is 64.8 kpc on a side.

Plummer models have parameters $M_{P1} = 9.3 \times 10^9 M_\odot$, $b_1 = 0.8$ kpc and $M_{P2} = 1.6 \times 10^{10} M_\odot$, $b_2 = 4.5$ kpc. For the double exponential bulge model, the two Plummer models have parameters $M_{P1} = 5.4 \times 10^9 M_\odot$, $b_1 = 0.6$ kpc and $M_{P2} = 1.7 \times 10^9 M_\odot$, $b_2 = 1.6$ kpc. For the $r^{1/4}$ bulge model, the disk component has a mass-to-light ratio of $M/L_H = 1.0$ in solar units, while the bulge model has $M/L_H = 1.5$. For the double exponential bulge model, the disk has $M/L_H = 0.85$ while the bulge has $M/L_H = 1.5$. For comparison, Salo et al. (1999) derived $M/L_H = 0.75$ for both the bulge and disk of IC 4214. Buta & Purcell (1998) derived $M/L_H = 0.8 \pm 0.1$ for NGC 3081, while Buta et al. (1998) obtained values of 0.5–2.4 for four other ringed galaxies. A single-burst, solar-metallicity population of age 12 Gyr has $M/L_H = 1.19$ (Worthey 1994). Oliva et al. (1995) summarize other M/L_H estimates for both spiral and elliptical galaxies.

The halo model we have used for both bulge-disk decompositions has $b = 41.1$ kpc and a mass of $2.26 \times 10^{11} M_\odot$ within the grid radius of 42.5 kpc. Beyond $140''$ we forced the total rotation curve to be constant, since Plummer models decline beyond $\sqrt{2}b$.

Figure 23 shows the variation of the angular rotation velocity, Ω , and the Lindblad precession frequencies, $\Omega \pm \kappa/2$, with radius inferred from the model rotation curve for the two bulge models. Here κ is the radial epicyclic frequency. The next step is to choose a pattern speed and then evolve the cloud-particle disk in the total potential, starting with only the axisymmetric component and then

turning on the nonaxisymmetric component slowly to avoid short-term transients. We experimented with pattern speeds in the range 8 to $40 \text{ km s}^{-1} \text{ kpc}^{-1}$.

The turn-on time for the nonaxisymmetric component is a fairly important parameter and is largely unknown. It cannot be too short, because the simulations will be subject to violent relaxation and transients (see Schwarz 1981; Sempere et al. 1995). However, it cannot be too long either because the gas is losing energy in collisions that is not being counterbalanced by star formation. We used a value of 450 Myr, which corresponds to about one bar rotation for the favored pattern speed (see below).

The results of the simulations suggest first that the pattern speed cannot be higher than the maximum of $\Omega - \kappa/2$, because then there is no inner Lindblad resonance and a nuclear ring does not form (see also Schwarz 1984; Byrd et al. 1994). For lower pattern speeds, a nuclear ring forms in the region between two allowed inner Lindblad resonances. Second, the extreme size of the ring may be connected to the broadness of the inner parts of the $\Omega - \kappa/2$ curve, which has an extended hump due to the inner bump in the disk rotation curve. Third, the extreme elongated shape of the nuclear ring seems to match the observed ring only at earlier time steps; at later time steps it evolves to rounder shapes, regardless of the turn-on time used. Finally, in all of the simulations we tried, the ring develops in a leading orientation to the bar but changes its orientation over time, to a perpendicular alignment and beyond.

We found that the size of the nuclear ring was most sensitive to pattern speed, but that size, shape, and orientation depended on time step as well. In deciding on the best choice for the pattern speed, we required that the predicted size of the ring when its shape and orientation were similar to that of the observed ring be within about 10% of the observed size. For a turn-on time of 450 Myr, this led to a pattern speed of $12 \pm 0.5 \text{ km s}^{-1} \text{ kpc}^{-1}$ for both bulge models. This range is shown as the shaded bands in Figures 23*b* and 23*d*.

Figures 24*a* and 24*b* show collision plot sequences for 16 time steps for the two bulge models. Both sets of simulations show the development of a strong elliptical nuclear ring and a much weaker inner ring (compare these plots with the deprojected *B*-band image in Fig. 25). No clear outer ring develops, but in the actual galaxy no ionized gas was detected from this feature either (BPC). For the $r^{1/4}$ bulge model, the two model rings resemble the observed ones in shape, size, and orientation for time steps 720 to 900 Myr. For the double exponential bulge model, the two rings achieve their correct sizes and shapes in the range 840 to 1020 Myr. The results are therefore not very sensitive to the adopted bulge model. Note that these models are not self-gravitating, do not allow for star formation, and in particular do not allow for gas replenishment of the ring, so they cannot be expected to provide an exact match to the observed galaxy.

Also shown in Figure 23 are the major axis radii of the observed nuclear ring (nr), inner pseudoring (rs), outer pseudoring (R'), and the bar. The models place corotation (CR) at nearly 2 times the bar radius, the inner pseudoring very close to the inner 4:1 resonance, and the outer pseudoring somewhat inside outer Lindblad resonance (OLR), although the position of the latter resonance is extremely sensitive to the treatment of the dark matter. The nuclear ring forms between two inner Lindblad resonances. The agreement with the observed features is surprising since neither the inner pseudoring nor the outer pseudoring has the alignment expected with the bar (parallel for the inner ring and perpendicular for the outer ring). Instead, these features are aligned parallel and perpendicular to the oval lens.

We made one final test of the models by carrying out a simulation where the $r^{1/4}$ bulge model was used as before but the disk light was deprojected for BPC's derived inclination of 33° . The mass-to-light ratio of the model, $M/L_H = 0.25$, was chosen to give a maximum rotation velocity of 100 km s^{-1} , consistent with the average of the two levels of rotation found by BPC. For a best-fitting pattern speed of $8 \text{ km s}^{-1} \text{ kpc}^{-1}$, the simulations again show the development of a nuclear ring between two ILRs having a diameter of about 5 kpc. However, the higher inclination makes the oval so important compared with the bar that only an open spiral forms outside the nuclear ring. We believe that the mass-to-light ratios obtained for the lower inclination models, which are consistent with those derived for single starburst models by Worthey (1994), as well as the gaseous morphologies in Figures 24*a* and 24*b*, argue against an inclination of 33° for ESO 565-11.

7. DISCUSSION

Elmegreen (1994) has elegantly described the theory of nuclear rings in barred galaxies. The idea is that galactic bars exert a strong negative torque on gas located inside CR

(see, e.g., Fig. 71*b* of Buta & Combes 1996), causing gas to accrete at an ILR. The accretion is not necessarily allowed to continue to the center but stalls at the ILR, forming a gas ring or spiral where the torques are in equilibrium. An inner inner Lindblad resonance, in the case of two ILRs, could add to the formation of the gas ring because of small leading spiral arms that can develop in that region (see Knapen et al. 1995*a*, 1995*b*; Sakamoto et al. 1995; Knapen 1996). A starburst can occur in a nuclear ring when the gas density exceeds a critical value depending on the square of the epicyclic frequency in the region of ILR. Once the critical density is exceeded, the ring can become gravitationally unstable to fragmentation, and several large star-forming clouds can develop along its circumference. Once the gas forms stars, the star formation can cease for a period until the density once again exceeds the critical value, and a new star-forming episode can ensue.

The nuclear ring of ESO 565-11 can easily fit into this theoretical framework. Our numerical simulations seem to firmly link the feature to the region between two ILRs, which is typically observed (see Buta & Combes 1996; Storchi-Bergmann, Wilson, & Baldwin 1996*b*) and which has also been predicted by more sophisticated high-resolution hydrodynamic models (Piner et al. 1995). The orientation of the nuclear ring at a significant angle to the bar can be explained in terms of the crossing of x_1 orbit families aligned along the bar with the x_2 family of orbits aligned perpendicular to the bar between the two ILRs (see Fig. 3 of Simkin, Su, & Schwarz 1980 and Fig. 60 of Buta & Combes 1996). The bar of ESO 565-11 is apparently weak enough that the x_2 family is strong and important. The size and shape of the ring may not be critical to the starburst but result strictly from the mass distribution and properties of orbits in the central region of ESO 565-11; a starburst probably could have occurred even if the ring were rounder, as in the case of NGC 6782 (Buta 1995). The lining of the ring by discrete massive super-star clusters suggests that fragmentation into massive molecular clouds occurred along the ring, with a few dominating the appearance of the ring. ESO 565-11 has not yet been observed in CO, but such observations will be needed to determine the molecular gas mass and density of some of the clouds.

Since star formation in the central region of a galaxy depends very critically on the density, such regions are not expected simply to form stars continuously, as in regions farther from the center where the actual gas density can more easily exceed the critical density. Instead, episodic star formation is favored in the region of ILR. We have noted that the extreme elongation of the nuclear ring of ESO 565-11 may be allowing us to determine directly what happens to stars born in the ring. Elmegreen (1994) suggests that once star formation ceases, the ILR ring will disperse. However, if the ring stars are born on a highly elongated oval oriented at a significant angle to the primary bar, then the bar should exert a torque on the stellar orbits, presumably in such a manner as to change their orientations to a more perpendicular alignment which would eliminate the torques. We believe there is evidence for this kind of change in the orientation of stellar isophotes underlying the ring region. If the *I* band highlights the oldest stellar population in our *HST* data, then that population has clearly dispersed within an oval aligned nearly perpendicular to the bar. The sense of the change, from an oval ring leading the bar to an oval zone perpendicular to the bar, is also consistent with

the way simulations show the gas nuclear ring to change, as well as with analytic calculations of the effects of dissipation on gas orbits (Byrd, Ousley, & Dalla Piazza 1998). Since the gas ring in ESO 565-11 forms stars, we do not see the young ring in a later stage of development where it becomes rounder or in a completely different alignment with the bar, as shown by the simulations.

The episodic idea of star formation in nuclear rings suggests that we might see a population of evolved clusters in the ring region if the time between episodes is short enough. As we have noted, we did not find strong evidence for such a population in the ring clusters of ESO 565-11. Very few red clusters are found compared with the striking population of red clusters found in NGC 7252 by Miller et al. (1997), and the red clusters we did find in ESO 565-11 are probably simply highly reddened young clusters from the current burst. Interestingly, Smith et al. (1999) found a displacement between the locations of radio bright knots and near-infrared bright knots in the nuclear ring of NGC 7771 that suggested two generations of star formation separated by about 6 Myr occurred in that case.

We have shown from two-color plots that the clusters in the nuclear ring of ESO 565-11 may be metal-rich compared with the Sun. This is not a firm conclusion, since it depends on the reliability of the aperture corrections, the transformation zero points, and ultimately the accuracy of the evolutionary synthesis models. However, a few nuclear rings have had abundances measured more directly that gives some support to this possibility. Storchi-Bergmann et al. (1996b) measured abundances in the nuclear rings of NGC 1097, 1672, and 5248, and found oxygen abundances about twice solar for the two cases (NGC 1097 and NGC 1672) including LINER nuclei and about 1.4 times solar for NGC 5248, a pure starburst case. Storchi-Bergmann et al. (1996a) derived oxygen abundances for two positions in the nuclear ring of NGC 1326 and obtained values slightly above solar. These authors also suggested that the nuclear region of NGC 3081, which includes a nuclear ring and a Seyfert nucleus, may be 4 times above solar in oxygen abundance. *HST* spectroscopy of the starburst nuclear ring region in the Seyfert NGC 1068 (Miskey et al. 1998) also indicated a metallicity about twice solar in that region. Other studies of the circumnuclear regions of Seyfert galaxies have indicated metallicities between 1 and 3 times solar (González-Delgado & Pérez 1996, 1997). These studies have tended to emphasize galaxies with active nuclei, while ESO 565-11 is mainly a starburst system. The tentative implication is that it may not be unreasonable that the clusters in the nuclear ring of ESO 565-11 are more metal-rich than the Sun.

Clearly, the nuclear ring of ESO 565-11 merits further study, in particular high-resolution H I, CO, and near-IR observations, as well as cluster abundance and extinction studies, are needed. More sophisticated numerical simulations could take into account self-gravity and probe the fragmentation and evolution of the ring. Only when more nuclear rings are analyzed in detail will it be possible to put the nuclear ring of ESO 565-11 into its proper perspective. Such studies are underway on numerous examples at this time (see, e.g., Maoz et al. 1998).

8. CONCLUSIONS

We have presented multiband *HST* imaging and photometry and near-infrared imaging and analysis of ESO

565-11, a peculiar barred spiral with the largest known example of a nuclear ring. The data have led to the following conclusions:

1. The nuclear ring of ESO 565-11 is populated with more than 700 clusters, most of which are probably less than 10 million years old. From the *V*-band luminosity function, the brightest clusters are clearly of the super-star cluster variety, having *V*-band absolute magnitudes of -12 to -14 . The slope of the luminosity function, $a = -2.18$, is typical of young cluster systems. There is no evidence for a population of redder and older clusters that might be associated with a previous burst. However, there appears to be an age spread of more than 1 Myr among the brighter clusters.

2. The ring of star clusters is easily separated from the background starlight. When so separated, the isophotes of the background starlight show a systematic change in position angle with increasing filter effective wavelength. The change is from an angle misaligned to the leading edge of the bar to an angle aligned nearly perpendicular to the bar. Based on azimuthal color changes along circles across the ring, we suggest that the change in orientation is due to the effect of gravity torques operating on aging ring stars.

3. The nuclear ring region includes a strong spiral dust pattern. However, this pattern does not clearly extend into the bar region. Star clusters are found on either side of the dust lanes, and the clusters define a true ring rather than a tight spiral.

4. The bulge region of ESO 565-11 is a well-defined circular object with some evidence of imbedded dust. The dust gives rise to an X-shaped pattern inside the bulge.

5. The near-infrared *H*-band light distribution was used to infer the disk gravitational potential in ESO 565-11, assuming a constant mass-to-light ratio. With Plummer representations of the bulge and halo, the potential was input into a sticky-particle dynamics code and a cloud-particle disk was evolved in the potential. A free parameter in the model was the pattern speed of the bar. The best models we obtained were for a pattern speed of $12 \pm 0.5 \text{ km s}^{-1} \text{ kpc}^{-1}$. In the models, the nuclear ring is associated with a broad region between two inner Lindblad resonances, and its existence depends on a strong family of x_2 periodic orbits. Its size, shape, and orientation match the observed ring parameters fairly early in the simulations. The extreme size and elongation of the ring may be due to the broadness of the $\Omega - \kappa/2$ function in the inner regions and the relative weakness of the bar. The model also predicts corotation to be at twice the radius of the bar and the inner ring to be located near the inner 4:1 resonance. The radius of the outer Lindblad resonance is not constrained reliably by these models.

The location of the nuclear ring in the region of inner Lindblad resonances is the most secure conclusion we have made from the simulations. This conclusion is independent of the bulge model used and of the assumed inclination.

This study benefited immensely from the *HST* observations of the nuclear ring region of ESO 565-11. We thank the Cycle 6 Time Allocation Committee for allocating us the three orbits that were needed. We also thank A. Quillen, F. Combes, A. Kalnajs, and S. Hughes for allowing us to use their programs for computing the dynamics of ESO 565-11, and for valuable discussions. Also, we thank an anonymous

referee for helpful suggestions that improved the paper. We acknowledge a grant from the Space Telescope Science Institute for financial support of this study. R. B. also

acknowledges NSF grant AST 96-17154 to the University of Alabama.

REFERENCES

- Arnaboldi, M., Capaccioli, M., Cappellaro, E., Held, E. V., & Koribalski, B. 1995, *AJ*, 110, 199
- Axon, D. J., & Robinson, A. 1996, in *Lecture Notes in Physics*, 474, *Barred Galaxies and Circumnuclear Activity*, ed. A. Sandqvist & P. O. Lindblad (New York: Springer), 223
- Barth, A. J., Ho, L. C., Filippenko, A. V., Gorjian, V., Malkan, M., & Sargent, W. L. W. 1996, in *IAU Colloq. 157, Barred Galaxies*, ed. R. Buta, D. A. Crocker, & B. G. Elmegreen (ASP Conf. Ser. 91) (San Francisco: ASP), 94
- Barth, A. J., Ho, L. C., Filippenko, A. V., & Sargent, W. L. W. 1995, *AJ*, 110, 1009
- Benedict, G. F., Howell, A., Jørgensen, I., Smith, B. J., & Kenney, J. D. P. 1998, *BAAS*, 192, No. 66.10
- Benedict, G. F., Smith, B. J., & Kenney, J. D. P. 1996, *AJ*, 111, 1861
- Binney, J., & Tremaine, S. 1987, *Galactic Dynamics* (Princeton: Princeton Univ. Press)
- Bruzual A., G., & Charlot, S. 1993, *ApJ*, 405, 538
- Burbidge, E. M., & Burbidge, G. R. 1960, *ApJ*, 132, 30
- Buta, R. J. 1984, Ph.D. thesis, Univ. Texas at Austin
- . 1995, *ApJS*, 96, 39 (CSRG)
- Buta, R., Alpert, A. J., Cobb, M. L., Crocker, D. A., & Purcell, G. B. 1998, *AJ*, 116, 1142
- Buta, R., & Combes, F. 1996, *Fundam. Cosmic Phys.*, 17, 95
- Buta, R., & Crocker, D. A. 1991, *AJ*, 102, 1715
- . 1992, *AJ*, 103, 1804
- . 1993, *AJ*, 105, 1344
- Buta, R., & Purcell, G. B. 1998, *AJ*, 115, 484
- Buta, R., Purcell, G. B., & Crocker, D. A. 1995, *AJ*, 110, 1588 (BPC)
- Byrd, G. G., Ousley, D., & Dalla Piazza, C. 1998, *MNRAS*, 298, 78
- Byrd, G., Rautiainen, P., Salo, H., Buta, R., & Crocker, D. A. 1994, *AJ*, 108, 476
- Caldwell, N., Kennicutt, R., Phillips, A. C., & Schommer, R. A. 1991, *ApJ*, 370, 526
- Cardelli, J. A., Clayton, G. C., & Mathis, J. S. 1989, *ApJ*, 345, 245
- Carlson, M. N., et al. 1998, *AJ*, 115, 1778
- Colina, L., García Vargas, M. L., Mas-Hesse, J. M., Alberdi, A., & Krabbe, A. 1997, *ApJ*, 484, L41
- Combes, F. 1993, in *N-Body Problems and Gravitational Dynamics*, ed. F. Combes & E. Athanassoula (Paris: Obs. Paris), 137
- Combes, F., & Gerin, M. 1985, *A&A*, 150, 327
- Combes, F., Gerin, M., Nakai, N., Kawabe, R., & Shaw, M. A. 1992, *A&A*, 259, L27
- Contini, T., Davoust, E., & Considère, S. 1995, *Astrophys. Lett. Commun.*, 31, 223
- Contini, T., Wozniak, H., Considère, S., & Davoust, E. 1997, *A&A*, 324, 41
- Crocker, D. A., Baugus, P. D., & Buta, R. 1996, *ApJS*, 105, 353
- de Vaucouleurs, G., de Vaucouleurs, A., Corwin, H. G., Jr., Buta, R., Paturel, G., & Fouqué, P. 1991, *Third Reference Catalogue of Bright Galaxies* (New York: Springer)
- Diaz, R., Carranza, R., Dottori, H., & Goldes, G. 1999, *ApJ*, 512, 623
- Elias, J. H., Frogel, J. A., Matthews, K., & Neugebauer, G. 1982, *AJ*, 87, 1029
- Elmegreen, B. G. 1994, *ApJ*, 425, L73
- Faber, S. M., et al. 1997, *AJ*, 114, 1771
- Forbes, D. A., Norris, R. P., Williger, G. M., & Smith, R. C. 1994, *AJ*, 107, 984
- Friedli, D. 1996, in *IAU Colloq. 157, Barred Galaxies*, ed. R. Buta, D. A. Crocker, & B. G. Elmegreen (ASP Conf. Ser. 91) (San Francisco: ASP), 378
- Friedli, D., Wozniak, H., Rieke, M., Martinet, L., & Bratschi, P. 1996, *A&AS*, 118, 461
- García-Barreto, J. A., Downes, D., Combes, F., Gerin, M., Magri, C., Carrasco, L., & Cruz-González, I. 1991, *A&A*, 244, 257
- González Delgado, R. M., & Pérez, E. 1996, *MNRAS*, 281, 781
- . 1997, *MNRAS*, 284, 931
- Graham, J. A. 1982, *PASP*, 94, 244
- Hawarden, T. G., Mountain, C. M., Leggett, S. K., & Puxley, P. J. 1986, *MNRAS*, 221, 41P
- Holtzman, J. A., Burrows, C. J., Casertano, S., Hester, J. J., Trauger, J. T., Watson, A. M., & Worthey, G. 1995a, *PASP*, 107, 1065
- Holtzman, J. A., et al. 1995b, *PASP*, 107, 156
- Hummel, E., van der Hulst, J. M., & Keel, W. C. 1987, *A&A*, 172, 32
- Kenney, J. D. P., Benedict, G. F., & Friedli, D. 1998, *BAAS*, 193, No. 53.03
- Kenney, J. D. P., Wilson, C. D., Scoville, N. Z., Devereux, N. A., & Young, J. S. 1992, *ApJ*, 395, L79
- Kennicutt, R. C., Jr. 1998, *ARA&A*, 36, 189
- Kennicutt, R. C., Jr., Edgar, B. K., & Hodge, P. W. 1989, *ApJ*, 337, 761
- Kent, S. M. 1986, *AJ*, 91, 1301
- Knapen, J. H. 1996, in *Lecture Notes in Physics*, 474, *Barred Galaxies and Circumnuclear Activity*, ed. A. Sandqvist & P. O. Lindblad (New York: Springer), 233
- Knapen, J. H. 1999, in *ASP Conf. Ser. 187, The Evolution of Galaxies and Cosmological Timescales*, ed. J. E. Beckman & T. J. Mahoney (San Francisco: ASP), in press
- Knapen, J. H., Beckman, J. E., Heller, C. H., Shlosman, I., & de Jong, R. S. 1995a, *ApJ*, 454, 623
- Knapen, J. H., Beckman, J. E., Shlosman, I., Peletier, R. F., Heller, C. H., & de Jong, R. S. 1995b, *ApJ*, 443, L73
- Knapen, J. H., Shlosman, I., Heller, C. H., Rand, R. J., Beckman, J. E., & Rozas, M. 2000, *ApJ*, in press
- Kohno, K., Kawabe, R., & Vila-Vilaró, B. 1999, *ApJ*, 511, 157
- Kormendy, J. 1977, *ApJ*, 217, 406
- Krist, J. 1995, in *ASP Conf. Ser. 77, Astronomical Data Analysis and Software Systems IV*, ed. R. A. Shaw, H. E. Payne, & J. J. E. Hayes (San Francisco: ASP), 349
- Landolt, A. U. 1992, *AJ*, 104, 340
- Lang, K. R. 1992, *Astrophysical Data*, Vol. 1, Planets and Stars (New York: Springer)
- Leitherer, C., et al. 1996, *PASP*, 108, 996
- Lejeune, T., Cuisinier, F., & Buser, R. 1996, in *AAS CD-ROM Series*, Vol. 7
- Maoz, D., Sternberg, A., & Ho, L. C. 1998, *BAAS*, 193, No. 76.04
- Miller, B. W., Whitmore, B. C., Schweizer, F., & Fall, S. M. 1997, *AJ*, 114, 2381
- Miskey, C. L., Bruhweiler, F. C., Smith Neubig, M., Landsman, W., Malamuth, E., & Smith, A. 1998, *BAAS*, 192, No. 69.07
- Morgan, W. W. 1958, *PASP*, 70, 364
- Oliva, E., Origlia, L., Kotilainen, J. K., & Moorwood, A. F. M. 1995, *A&A*, 301, 55
- Phillips, A. C., Illingworth, G. D., MacKenty, J. W., & Franx, M. 1996, *AJ*, 111, 1566
- Piner, B. G., Stone, J. M., & Teuben, P. J. 1995, *ApJ*, 449, 508
- Quillen, A. C., Frogel, J. A., & González, R. A. 1994, *ApJ*, 437, 162
- Rautiainen, P., Salo, H., Byrd, G., Buta, R., & Crocker, D. A. 1996, in *IAU Colloq. 157, Barred Galaxies*, ed. R. Buta, D. A. Crocker, & B. G. Elmegreen (ASP Conf. Ser. 91) (San Francisco: ASP), 483
- Rubin, V. C., Ford, W. K., Jr., & Peterson, C. J. 1975, *ApJ*, 199, 39
- Salo, H., Rautiainen, P., Buta, R., Purcell, G. B., Cobb, M. L., Crocker, D. A., & Laurikainen, E. 1999, *AJ*, 117, 792
- Salpeter, E. E. 1955, *ApJ*, 121, 161
- Sakamoto, K., Okumura, S., Minezaki, T., Kobayashi, Y., & Wada, K. 1995, *AJ*, 110, 2075
- Sandage, A. R. 1961, *The Hubble Atlas of Galaxies* (Washington: Carnegie Inst. Washington)
- Scalo, J. M. 1986, *Fundam. Cosmic Phys.*, 11, 1
- Schinnerer, E., Eckart, A., Quirrenbach, A., Böker, T., Tacconi-Garman, L. E., Krabbe, A., & Sternberg, A. 1997, *ApJ*, 488, 174
- Schwarz, M. P. 1981, *ApJ*, 247, 77
- . 1984, *MNRAS*, 209, 93
- Schweizer, F. 1980, *ApJ*, 237, 303
- . 1999, *BAAS*, 194, No. 40.10
- Sellwood, J. A., & Wilkinson, A. 1993, *Rep. Prog. Phys.*, 56, 173
- Sempere, M. J., García-Burillo, S., Combes, F., & Knapen, J. H. 1995, *A&A*, 296, 45
- Sérsic, J. L., & Pastoriza, M. 1965, *PASP*, 77, 287
- . 1967, *PASP*, 79, 152
- Shaw, M., Combes, F., Axon, D. J., & Wright, G. S. 1993, *A&A*, 273, 31
- Shlosman, I., Frank, J., & Begelman, M. C. 1989, *Nature*, 338, 45
- Simkin, S., Su, H. J., & Schwarz, M. P. 1980, *ApJ*, 237, 404
- Smith, D. A., Herter, T., Haynes, M. P., & Neff, S. G. 1995, *BAAS*, 186, No. 40.04
- . 1999, *ApJ*, 510, 669
- Stetson, P. B. 1987, *PASP*, 99, 191
- Storchi-Bergmann, T., Rodríguez-Ardila, A., Schmitt, H. R., Wilson, A. S., & Baldwin, J. A. 1996a, *ApJ*, 472, 83
- Storchi-Bergmann, T., Wilson, A. S., & Baldwin, J. A. 1996b, *ApJ*, 460, 252
- Telesco, C. M., Dressel, L. L., & Wolstencroft, R. D. 1993, *ApJ*, 414, 120
- Tully, R. B., Pierce, M. J., Huang, J.-S., Saunders, W., Verheijen, M. A. W., & Witchalls, P. L. 1998, *AJ*, 115, 2264
- van Moorsel, G. A., & Wells, D. C. 1985, *AJ*, 90, 1038
- Vega Beltrán, J. C., Zeilinger, W. W., Amico, P., Schultheis, M., Corsini, E. M., Funes, J. G., Beckman, J., & Bertola, F. 1998, *A&AS*, 131, 105
- Whitmore, B. 1995, in *Calibrating Hubble Space Telescope: Post Servicing Mission*, ed. A. Koratkar & C. Leitherer (Baltimore: STScI), 269
- Whitmore, B., & Heyer, I. 1997, *New Results on Charge Transfer Efficiency and Constraints on Flat-Field Accuracy (WFPC2 Instrum. Sci. Rep. 97-08)* (Baltimore: STScI)
- Whitmore, B. C., & Schweizer, F. 1995, *AJ*, 109, 960
- Wilson, A. S., Helfer, T. T., Haniff, C. A., & Ward, M. J. 1991, *ApJ*, 381, 79
- Worthey, G. 1994, *ApJS*, 95, 107
- Wozniak, H., Friedli, D., Martinet, L., Martin, P., & Bratschi, P. 1995, *A&AS*, 111, 115